

Sandra Siljeström and Andrew Czaja  
contributed equally to this work.

### Key Points:

- Sulfate phases detected by Scanning Habitable Environments with Raman and Luminescence for Organics and Chemistry and PIXL in igneous units consists of crystalline/amorphous Mg-sulfate minerals with 3–5 waters and anhydrous Ca-sulfate minerals
- Hydration of sulfate minerals sets a lower constraint on how much subsurface water is stored in sulfate minerals
- The sulfate minerals of Jezero crater floor were deposited in moderate pH, likely at low temperature, and during several episodes

### Supporting Information:

Supporting Information may be found in the online version of this article.

### Correspondence to:

S. Siljeström and A. D. Czaja,  
[sandra.siljstrom@ri.se](mailto:sandra.siljstrom@ri.se);  
[andrew.czaja@uc.edu](mailto:andrew.czaja@uc.edu)

### Citation:

Siljeström, S., Czaja, A. D., Corpolongo, A., Berger, E. L., Li, A. Y., Cardarelli, E., et al. (2024). Evidence of sulfate-rich fluid alteration in Jezero Crater Floor, Mars. *Journal of Geophysical Research: Planets*, 129, e2023JE007989. <https://doi.org/10.1029/2023JE007989>

Received 31 JUL 2023






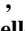







Accepted 23 DEC 2023

### Author Contributions:

**Conceptualization:** Sandra Siljeström, Andrew D. Czaja, Luther W. Beegle, Rohit Bhartia, Ryan Roppel

© 2024 Jet Propulsion Laboratory, California Institute of Technology. Journal of Geophysical Research: Planets published by Wiley Periodicals LLC on behalf of American Geophysical Union. This is an open access article under the terms of the [Creative Commons Attribution-NonCommercial License](https://creativecommons.org/licenses/by/4.0/), which permits use, distribution and reproduction in any medium, provided the original work is properly cited and is not used for commercial purposes.

## Evidence of Sulfate-Rich Fluid Alteration in Jezero Crater Floor, Mars

Sandra Siljeström<sup>1</sup> , Andrew D. Czaja<sup>2</sup> , Andrea Corpolongo<sup>2</sup> , Eve L. Berger<sup>3</sup>, An Y. Li<sup>4</sup>, Emily Cardarelli<sup>5</sup> , William Abbey<sup>5</sup> , Sanford A. Asher<sup>6</sup>, Luther W. Beegle<sup>5</sup>, Kathleen C. Benison<sup>7</sup> , Rohit Bhartia<sup>8</sup> , Benjamin L. Bleefeld<sup>9</sup>, Aaron S. Burton<sup>3</sup> , Sergei V. Bykov<sup>6</sup> , Benton Clark<sup>10</sup> , Lauren DeFlores<sup>5</sup>, Bethany L. Ehlmann<sup>11</sup> , Teresa Fornaro<sup>12</sup> , Allie Fox<sup>13,14</sup> , Felipe Gómez<sup>15</sup> , Kevin Hand<sup>5</sup> , Nikole C. Haney<sup>13</sup> , Keyron Hickman-Lewis<sup>16,17</sup>, William F. Hug<sup>8</sup>, Samara Imbeah<sup>9</sup>, Ryan S. Jakubek<sup>13</sup>, Linda C. Kah<sup>18</sup> , Lydia Kivrak<sup>19</sup>, Carina Lee<sup>13,14</sup>, Yang Liu<sup>5</sup> , Jesús Martínez-Frías<sup>20</sup> , Francis M. McCubbin<sup>3</sup> , Michelle Miniti<sup>21</sup> , Kelsey Moore<sup>5</sup>, Richard V. Morris<sup>3</sup> , Jorge I. Núñez<sup>22</sup> , Jeffrey T. Osterhout<sup>5</sup>, Yu Yu Phua<sup>11</sup> , Nicolas Randazzo<sup>23</sup>, Joseph Razzell Hollis<sup>16</sup>, Carolina Rodriguez<sup>9</sup> , Ryan Roppel<sup>6</sup> , Eva L. Scheller<sup>24</sup>, Mark Sephton<sup>25</sup> , Shiv K. Sharma<sup>26</sup> , Sunanda Sharma<sup>5</sup>, Kim Steadman<sup>5</sup> , Andrew Steele<sup>27</sup>, Michael Tice<sup>28</sup>, Kyle Uckert<sup>5</sup> , Scott VanBommel<sup>29</sup>, Amy J. Williams<sup>19</sup> , Kenneth H. Williford<sup>30</sup>, Katherine Winchell<sup>9,31</sup>, Megan Kennedy Wu<sup>9</sup>, Anastasia Yanchilina<sup>32</sup> , and Maria-Paz Zorzano<sup>15</sup> 

<sup>1</sup>RISE Research Institutes of Sweden, Stockholm, Sweden, <sup>2</sup>Department of Geosciences, University of Cincinnati, Cincinnati, OH, USA, <sup>3</sup>NASA Johnson Space Center, Houston, TX, USA, <sup>4</sup>Department of Earth and Space Sciences/Astrobiology Program, University of Washington, Seattle, WA, USA, <sup>5</sup>Jet Propulsion Laboratory, California Institute of Technology, Pasadena, CA, USA, <sup>6</sup>Department of Chemistry, University of Pittsburgh, Pittsburgh, PA, USA, <sup>7</sup>Department of Geology and Geography, West Virginia University, Morgantown, WV, USA, <sup>8</sup>Photon Systems Inc., Covina, CA, USA, <sup>9</sup>Malin Space Science Systems, San Diego, CA, USA, <sup>10</sup>Space Science Institute, Boulder, CO, USA, <sup>11</sup>Division of Geological and Planetary Sciences, California Institute of Technology, Pasadena, CA, USA, <sup>12</sup>INAF-Astrophysical Observatory of Arcetri, Florence, Italy, <sup>13</sup>Jacobs JETS, NASA Johnson Space Center, Houston, TX, USA, <sup>14</sup>LPI, Houston, TX, USA, <sup>15</sup>Centro de Astrobiología (CAB), CSIC-INTA, Madrid, Spain, <sup>16</sup>The Natural History Museum, London, UK, <sup>17</sup>Dipartimento di Scienze Biologiche, Geologiche e Ambientali, Università di Bologna, Bologna, Italy, <sup>18</sup>Department of Earth and Planetary Sciences, University of Tennessee, Knoxville, TN, USA, <sup>19</sup>Department of Geological Sciences, University of Florida, Gainesville, FL, USA, <sup>20</sup>Institute of Geosciences, IGEO (CSIC-UCM), Madrid, Spain, <sup>21</sup>Framework, Silver Spring, MD, USA, <sup>22</sup>Johns Hopkins University Applied Physics Laboratory, Laurel, MD, USA, <sup>23</sup>Department of Earth and Atmospheric Sciences, University of Alberta, Edmonton, AB, Canada, <sup>24</sup>Department of Earth, Atmospheric, and Planetary Sciences, MIT, Cambridge, MA, USA, <sup>25</sup>Imperial College London, London, UK, <sup>26</sup>Hawaii Institute of Geophysics & Planetology, University of Hawaii, Honolulu, HI, USA, <sup>27</sup>Carnegie Institution of Washington, Washington, DC, USA, <sup>28</sup>Texas A&M University, College Station, TX, USA, <sup>29</sup>Department of Earth and Planetary Sciences, Washington University in St. Louis, St. Louis, MO, USA, <sup>30</sup>Blue Marble Space Institute of Science, Seattle, WA, USA, <sup>31</sup>Arizona State University, Tempe, AZ, USA, <sup>32</sup>Impossible Sensing, LLC, St. Louis, MO, USA

**Abstract** Sulfur plays a major role in martian geochemistry and sulfate minerals are important repositories of water. However, their hydration states on Mars are poorly constrained. Therefore, understanding the hydration and distribution of sulfate minerals on Mars is important for understanding its geologic, hydrologic, and atmospheric evolution as well as its habitability potential. NASA's Perseverance rover is currently exploring the Noachian-age Jezero crater, which hosts a fan-delta system associated with a paleolake. The crater floor includes two igneous units (the Séítah and Mááz formations), both of which contain evidence of later alteration by fluids including sulfate minerals. Results from the rover instruments Scanning Habitable Environments with Raman and Luminescence for Organics and Chemistry and Planetary Instrument for X-ray Lithochemistry reveal the presence of a mix of crystalline and amorphous hydrated Mg-sulfate minerals (both  $\text{MgSO}_4 \cdot [3-5]\text{H}_2\text{O}$  and possible  $\text{MgSO}_4 \cdot \text{H}_2\text{O}$ ), and anhydrous Ca-sulfate minerals. The sulfate phases within each outcrop may have formed from single or multiple episodes of water activity, although several depositional events seem likely for the different units in the crater floor. Textural and chemical evidence suggest that the sulfate minerals most likely precipitated from a low temperature sulfate-rich fluid of moderate pH. The identification of approximately four waters puts a lower constraint on the hydration state of sulfate minerals in the shallow subsurface, which has implications for the martian hydrological budget. These sulfate minerals are key samples for future Mars sample return.

**Data curation:** Sandra Siljeström, Andrew D. Czaja, Rohit Bhartia, Kevin Hand, Kyle Uckert

**Formal analysis:** Sandra Siljeström, Andrew D. Czaja, Andrea Corpolongo, An Y. Li, Sanford A. Asher, Rohit Bhartia, Bethany L. Ehlmann, Teresa Fornaro, Allie Fox, Felipe Gómez, Nikole C. Haney, Ryan S. Jakubek, Linda C. Kah, Lydia Kivrak, Yang Liu, Jesús Martínez-Frías, Francis M. McCubbin, Michelle Minitti, Richard V. Morris, Jorge I. Núñez, Jeffrey T. Osterhout, Yu Yu Phua, Nicolas Randazzo, Joseph Razzell Hollis, Ryan Roppel, Eva L. Scheller, Mark Sephton, Sunanda Sharma, Andrew Steele, Michael Tice, Amy J. Williams, Kenneth H. Williford, Anastasia Yanchilina, Maria-Paz Zorzano

**Investigation:** Sandra Siljeström, Andrew D. Czaja, Andrea Corpolongo, Eve L. Berger, An Y. Li, Emily Cardarelli, William Abbey, Luther W. Beegle, Kathleen C. Benison, Rohit Bhartia, Benjamin L. Bleefeld, Aaron S. Burton, Sergei V. Bykov, Benton Clark, Lauren DeFlores, Bethany L. Ehlmann, Teresa Fornaro, Allie Fox, Felipe Gómez, Kevin Hand, Nikole C. Haney, Keyron Hickman-Lewis, Samara Imbeah, Ryan S. Jakubek, Linda C. Kah, Lydia Kivrak, Carina Lee, Yang Liu, Francis M. McCubbin, Michelle Minitti, Kelsey Moore, Richard V. Morris, Jorge I. Núñez, Jeffrey T. Osterhout, Yu Yu Phua, Nicolas Randazzo, Joseph Razzell Hollis, Carolina Rodriguez, Ryan Roppel, Eva L. Scheller, Shiv K. Sharma, Sunanda Sharma, Kim Steadman, Andrew Steele, Michael Tice, Scott VanBommel, Amy J. Williams, Kenneth H. Williford, Katherine Winchell, Megan Kennedy Wu, Anastasia Yanchilina, Maria-Paz Zorzano

**Methodology:** Sandra Siljeström, Andrew D. Czaja, Andrea Corpolongo, Eve L. Berger, An Y. Li, William Abbey, Sanford A. Asher, Luther W. Beegle, Rohit Bhartia, Benjamin L. Bleefeld, Aaron S. Burton, Sergei V. Bykov, Bethany L. Ehlmann, Kevin Hand, William F. Hug, Samara Imbeah, Ryan S. Jakubek, Michelle Minitti, Kelsey Moore, Richard V. Morris, Yu Yu Phua, Joseph Razzell Hollis, Ryan Roppel, Sunanda Sharma, Andrew Steele, Michael Tice, Kyle Uckert, Scott VanBommel, Katherine Winchell, Megan Kennedy Wu

**Project Administration:** Sandra Siljeström, Andrew D. Czaja, Luther W. Beegle, Rohit Bhartia, Kevin Hand, Kyle Uckert

**Software:** Michael Tice, Kyle Uckert

**Supervision:** Luther W. Beegle, Rohit Bhartia, Kevin Hand, Kyle Uckert

**Visualization:** Sandra Siljeström, Andrew D. Czaja, Andrea Corpolongo, Eve L. Berger, An Y. Li, Michael Tice

**Writing – original draft:** Sandra Siljeström, Andrew D. Czaja, Emily Cardarelli, Kathleen C. Benison, Rohit Bhartia, Jesús Martínez-Frías, Mark Sephton, Amy J. Williams

**Plain Language Summary** The history of water on Mars is a puzzle that is of interest to scientists as well as the general public. Mars currently has water in the form of ice at the poles, trace amounts of gas in the atmosphere, and an unknown amount beneath the surface as ground water, bound in minerals, and in ice. However, there is strong evidence that ancient Mars may have had long-lived streams, rivers, and lakes. There is still much to learn about what Mars was like and how it transformed over time. One approach is to study the inventory of water at different times. In this work, we report the presence of hydrated magnesium sulfate (similar to Epsom salts) and dehydrated calcium sulfate that were formed by water flowing through cracks in volcanic rocks at the bottom of the 3.8-billion-year-old Jezero crater. These hydrated minerals trap water within themselves and record the history of how and when they formed. Returning samples of these minerals to Earth would allow researchers to explore the history of Mars' water and climate, and possibly evidence of ancient life with the most sensitive instruments possible.

## 1. Introduction

The Perseverance rover is exploring Jezero crater located at the edge of Isidis Planitia on Mars. Orbital data constrain the age of Jezero crater's formation to between 3.82 and 3.96 billion years (Mandon et al., 2020; Werner, 2008). The crater's two inlet channels and a discrete outlet valley as well as two depositional fans suggest that it was the site of a paleolake (Fassett & Head, 2005; Goudge et al., 2015; Schon et al., 2012). The Jezero western fan and associated deltaic deposits are estimated to be ~3.5 billion years old and represent the youngest unit of the Jezero crater (Mangold et al., 2020). The rover landing site is on the crater floor, made up of a series of units that underlie and are therefore older than the sedimentary deltaic deposits (Holm-Alwmark et al., 2021; Sun & Stack, 2020). Orbital data indicate the widespread occurrence of minerals formed by the interaction of water with rocks in Jezero crater, such as phyllosilicate minerals, although there is a lack of orbital detection of sulfate phases in this location (Ehlmann & Edwards, 2014). This paper discusses the presence and origin of sulfate phases in the Jezero crater floor detected by the Perseverance rover.

### 1.1. Payload and Goals of the Perseverance Rover

The Perseverance rover hosts six instruments to investigate the geology and environment of the Jezero crater region, including via multispectral imaging and macro- to micro-scale resolved chemical characterization. These instruments and the data sets they produce enable the key science goals of the Mars 2020 mission: (a) seek signs of ancient life within Mars, (b) characterize the processes of climate and its history on Mars, (c) understand the origin and evolution of Mars as a geologic system, and (d) prepare for human exploration (Farley et al., 2020; Williford et al., 2018). Another key objective of the Mars 2020 mission is to collect samples for potential future return to Earth that can also be used to address these goals.

The mast instruments on Perseverance (MastCam-Z or ZCAM, and SuperCam) provide large-scale geomorphology and chemistry to provide geological context. In addition, the rover includes two arm-mounted proximity instruments that operate at centimeter standoff distances with sub-millimeter resolution. The Scanning Habitable Environments with Raman and Luminescence for Organics and Chemicals (SHERLOC) and Planetary Instrument for X-ray Lithochemistry (PIXL) provide complementary in situ spatially resolved mineral, chemical and textural data of investigated rocks (see Sections 2.2 and 2.3).

### 1.2. Jezero Crater Floor Geologic Context

On Mars 2020 mission sol 380 (a sol is a martian day), Perseverance completed the Crater Floor Campaign. In situ observations of the lithology, stratigraphy, and mineralogy using the Perseverance payload enabled the redefinition of the original crater units (defined from orbital data by Stack et al., 2020) as the Séítah formation (formerly Cf-f-1) and the Máaz formation (formerly Cf-fr) (Farley et al., 2022; Sun et al., 2023). The Séítah formation is interpreted to be an olivine cumulate carbonated under low water/rock conditions (Farley et al., 2022; Liu et al., 2022; Scheller et al., 2022; Tice et al., 2022) and includes multiple layers of varying composition. The Máaz formation is interpreted to be an igneous unit having a basaltic to basaltic-andesitic composition (Udry et al., 2023). The Séítah formation has been divided into three units, all belonging to the Bastide member, listed in ascending stratigraphic order: Brac, Bastide, and Issole (Beysac et al., 2023). A fourth unit, the Content member, sits above the others in the Séítah formation, but its stratigraphic relationship is uncertain. The Máaz

**Writing – review & editing:** Sandra Siljeström, Andrew D. Czaja, Andrea Corpolongo, An Y. Li, Emily Cardarelli, Kathleen C. Benison, Rohit Bhartia, Sergei V. Bykov, Bethany L. Ehlmann, Teresa Fornaro, Kevin Hand, Nikole C. Haney, Keyron Hickman-Lewis, Ryan S. Jakubek, Linda C. Kah, Lydia Kivrak, Carina Lee, Yang Liu, Francis M. McCubbin, Kelsey Moore, Richard V. Morris, Jorge I. Núñez, Jeffrey T. Osterhout, Yu Yu Phua, Nicolas Randazzo, Joseph Razzell Hollis, Ryan Roppel, Eva L. Scheller, Mark Sephton, Shiv K. Sharma, Sunanda Sharma, Andrew Steele, Michael Tice, Kyle Uckert, Scott VanBommel, Amy J. Williams, Kenneth H. Williford, Anastasia Yanchilina, Maria-Paz Zorzano

formation is divided into five members listed from oldest to youngest: Artuby, Rochette, Roubion, Naa'táanii, and Ch'al (Horgan et al., 2023). The stratigraphic relationship between the two formations suggests that Séítah is older than Mááz, and both are older than the delta (Farley et al., 2022; Hamran et al., 2022; Sun & Stack, 2020; Sun et al., 2023).

### 1.3. Alteration of Igneous Units and Sulfate Mineralogy

A major unresolved question within these units is how and when their primary members undergo alteration processes since deposition. The chemical and textural heterogeneity of the Séítah and Mááz formations differs from prior observations of martian igneous units identified in earlier missions and landing sites, which suggests a potentially complex magmatic and alteration history (Udry et al., 2023). Thus, understanding the formation and later aqueous alteration of the Séítah and Mááz formations is pivotal to elucidating the geologic context of Jezero crater. The presence of secondary minerals has been reported previously in both the Séítah and Mááz formations in the form of sulfate phases, low (Fe, Mg) silicate phases, Mg- and Fe-phylosilicate minerals, Fe-oxyhydroxide phases, and perchlorate phases, whereas carbonate phases were mainly present in the Séítah formation, with uncertain detection in the Mááz formation (Corpolongo et al., 2023; Mandon et al., 2023; Scheller et al., 2022; Tice et al., 2023). Both the Séítah and Mááz formations are interpreted to have undergone multiple aqueous alteration events given the detection of interspersed sulfate, carbonate, and perchlorate/chlorate phases (Razzell Hollis et al., 2022; Scheller et al., 2022; Tice et al., 2022). In addition, the SHERLOC instrument detected fluorescence features that are spatially associated with sulfate phases in rocks of the Jezero crater floor (Sharma et al., 2023).

Sulfate phases are ubiquitous at the surface of Mars, as identified by both orbital and in situ rover-based observations (e.g., Ehlmann & Edwards, 2014; Wang et al., 2016). Sulfate minerals typically occur within Martian dust and soils (e.g., B. C. Clark & Van Hart, 1981; Kounaves et al., 2010; Wang, Haskin, et al., 2006); in light-toned deposits present inside canyons, in chaos terrain, and within sedimentary rocks of Meridiani Planum (e.g., Ehlmann & Edwards, 2014; Gendrin et al., 2005; Wang et al., 2016); as evaporites or diagenetic precipitates in sedimentary rocks (e.g., McLennan et al., 2005; Rapin et al., 2019); and as mineralized veins that cross-cut local stratigraphy (e.g., Kronyak et al., 2019; Nachon et al., 2014). In Jezero crater, sulfate phases have been detected in igneous units (Corpolongo et al., 2023; Mandon et al., 2023), regolith targets (Hausrath et al., 2023), and recently in the fan front (Hurowitz et al., 2023; Phua et al., 2023; Roppel et al., 2023). Sulfate minerals can hold water in two ways: (a) as part of the crystal structure in the case of hydrated sulfate phases, and (b) as fluid inclusions within sulfate crystals. Due to their capability to contain water, sulfate minerals are potentially large reservoirs of water and are therefore important for understanding the hydrological cycle on Mars. For instance, sulfate phases have been proposed to explain large hydrogen detections by the Mars Odyssey gamma ray spectrometer (Feldman, Mellon, et al., 2004; Feldman, Prettyman, et al., 2004; Karunatillake et al., 2014, 2016).

Orbital observations suggest that the sulfate phases found globally across Mars consists primarily of monohydrated Mg-sulfate and polyhydrated sulfate phases (e.g., Mg- and/or Fe-sulfate minerals and gypsum) (Ehlmann & Edwards, 2014; Gendrin et al., 2005; Karunatillake et al., 2016; Wang et al., 2016). In addition, in situ rover-based measurements have identified Mg-sulfate minerals, Ca-sulfate minerals such as anhydrite, bassanite, and gypsum, as well as the Fe-sulfate mineral jarosite on the surface on Mars (Klingelhöfer et al., 2004; Morris et al., 2006; Rapin et al., 2019; Vaniman et al., 2018; Wang, Haskin, et al., 2006). Furthermore, martian meteorites also host numerous sulfate phases that are thought to have formed on Mars, including anhydrite, gypsum, and jarosite (Bridges et al., 2001; McCubbin et al., 2009). However, the exact hydration state of the polyhydrated sulfate phases identified from the orbit is difficult to constrain, and recent results from the Curiosity rover suggest that some polyhydrated sulfate phases in Gale crater are amorphous (Rampe et al., 2020; Smith et al., 2022).

Sulfate, perchlorate, and chloride salts can extract water from (and release it to) the atmosphere under present-day martian environmental conditions either by undergoing hydration, deliquescence, or by forming liquid brines (Gough et al., 2011; Martin-Torres et al., 2015; Toner et al., 2016; Zorzano et al., 2009). Perseverance's instruments have detected the presence of hydrated Ca- and Mg-sulfate minerals in Jezero crater rocks (Corpolongo et al., 2023; Mandon et al., 2023) and regolith targets (Hausrath et al., 2023). Observations by the Perseverance instrument Mars Environmental Dynamics Analyzer (MEDA) indicate the possibility of diurnal and seasonal changes in the hydration of Mg-sulfate and Ca-sulfate salts (Hausrath et al., 2023).

There are several hypotheses for how sulfate phases might have formed on Mars, including (a) direct precipitation from sulfate-rich surface water, groundwater, and hydrothermal fluids; (b) acid-sulfate dissolution whereby

acid-sulfate brines/groundwater dissolve host rocks and precipitate sulfate minerals; and (c) interactions between basaltic rocks and volcanic-derived acidic volatiles, including aerosols or dissolved volatiles (acid-fog model) (Andrews-Hanna et al., 2007; Banin et al., 1997; Dehouck et al., 2012; Moore & Szykiewicz, 2023; Rapin et al., 2019; Tosca et al., 2004). Based on morphological evidence provided during ground-based research, the first two mechanisms occurred (e.g., McLennan et al., 2005; Morris et al., 2006; Rapin et al., 2019), although evidence for the third is present within at least one martian meteorite (McCubbin et al., 2009).

In this paper, we use SHERLOC and PIXL data to investigate the nature of the sulfate minerals detected in the igneous units of the Jezero crater floor, including their hydration states, their relationship to other alteration minerals and fluorescence signals detected, and interpret their origin.

## 2. Materials and Methods

### 2.1. Abrasion Targets

Perseverance is equipped with an abrasion bit to remove the outer few millimeters (typically 7–10 mm) from an area ~5 cm wide from the targets of interest. Abrading provides a petrographic window into the lithology and stratigraphy of the geologic members of the formations by removing the recent surface alteration and weathering, and providing a flat and dust-free surface, enabling in situ analyses and interpretation of rock faces during the mission. Unobstructed views of fresh rock surfaces and their chemical and mineralogical interpretations contribute to decisions of core collection of the same material for potential return to Earth.

During the crater floor campaign, seven outcrops of the various members of the Séítah and Máaz formations were targeted for abrasion (Simon et al., 2023; Sun et al., 2023). The Séítah formation abrasions include (from stratigraphically low to high) Garde (Bastide outcrop), Dourbes (Brac outcrop), and Quartier (Issole outcrop). The Máaz formation abrasions include (from stratigraphically low to high) Montpezat (Artuby outcrop), Bellegarde (Rochette outcrop), Guillaumes (Roubion outcrop), and Alfalfa (Ch'al outcrop) (Figure 1; Beyssac et al., 2023; Horgan et al., 2023). SHERLOC identified sulfate phases in four of the seven abrasions made on the Séítah and Máaz formations of the crater floor, namely Dourbes, Quartier, Bellegarde, and Guillaumes (Corpolongo et al., 2023). PIXL detected sulfate in each of these ( $\text{SO}_3 > 2$  wt%) and only smaller quantities of sulfate minerals in Montpezat and Alfalfa ( $\text{SO}_3 < 1$  wt%). Three of the four abrasion targets within which SHERLOC detected sulfate minerals also had co-registered PIXL scans (Dourbes, Quartier, and Bellegarde). Both SHERLOC and PIXL scans were performed on the fourth target (Guillaumes), but they did not overlap.

### 2.2. Description of SHERLOC

The Scanning Habitable Environments with Raman and Luminescence for Organics and Chemicals (SHERLOC) instrument was used to detect and classify minerals and organic molecules in a microtextural context via resonance Raman and native fluorescence spectroscopy. The details of the instrument and specifications are described by Bhartia et al. (2021). Briefly, the SHERLOC instrument consists of two boresights. One is the Wide Angle Topographic Sensor for Operations and eNginEering (WATSON) camera, modeled after the Mars Hand Lens Imager (MAHLI) camera on the Curiosity rover (Bhartia et al., 2021; Edgett et al., 2012; Wogsland et al., 2023). The other boresight is a deep UV fluorescence and Raman mapping spectrometer coupled to a co-boresighted Autofocus Context Imager (ACI), which is a grayscale microscopic imager with 10.1  $\mu\text{m}/\text{pixel}$  resolution that is used for focusing the spectrometer as well as providing textural context for the spectral maps. WATSON is a color imager that images at working distances of ~1.8 cm to infinity with a spatial resolution ranging from approximately 16–160  $\mu\text{m}/\text{pixel}$  for working distances associated with proximity science (a few to tens of centimeters). Images associated with proximity science include full views of the abrasions (e.g., Figure 1) as well as “hand lens”-scale images and are used for grain-scale textural information and to colorize the ACI images (Sharma et al., 2023). The SHERLOC spectrometer uses a 248.6 nm NeCu deep UV laser to induce Raman scatter (810–3,500  $\text{cm}^{-1}$ ) and fluorescence emission (274–365 nm) and uses a single CCD (charge-coupled detector) to detect both spectral phenomena simultaneously. Although the SHERLOC spectrometer is sensitive down to 400  $\text{cm}^{-1}$ , the signal in the spectrum region lower than 810  $\text{cm}^{-1}$  is attenuated by the internal optics. Two-dimensional spectral maps are generated by using an integrated scanner to raster the 106  $\mu\text{m}$  diameter laser beam focal annulus over a surface. At each analysis point, 15 to 500 laser pulses were used to collect spectra.

Although the SHERLOC instrument has a variety of possible operational parameters, for the efforts discussed here, we largely focus on the two primary scan types, referred to as High Dynamic Range (HDR) and Detail



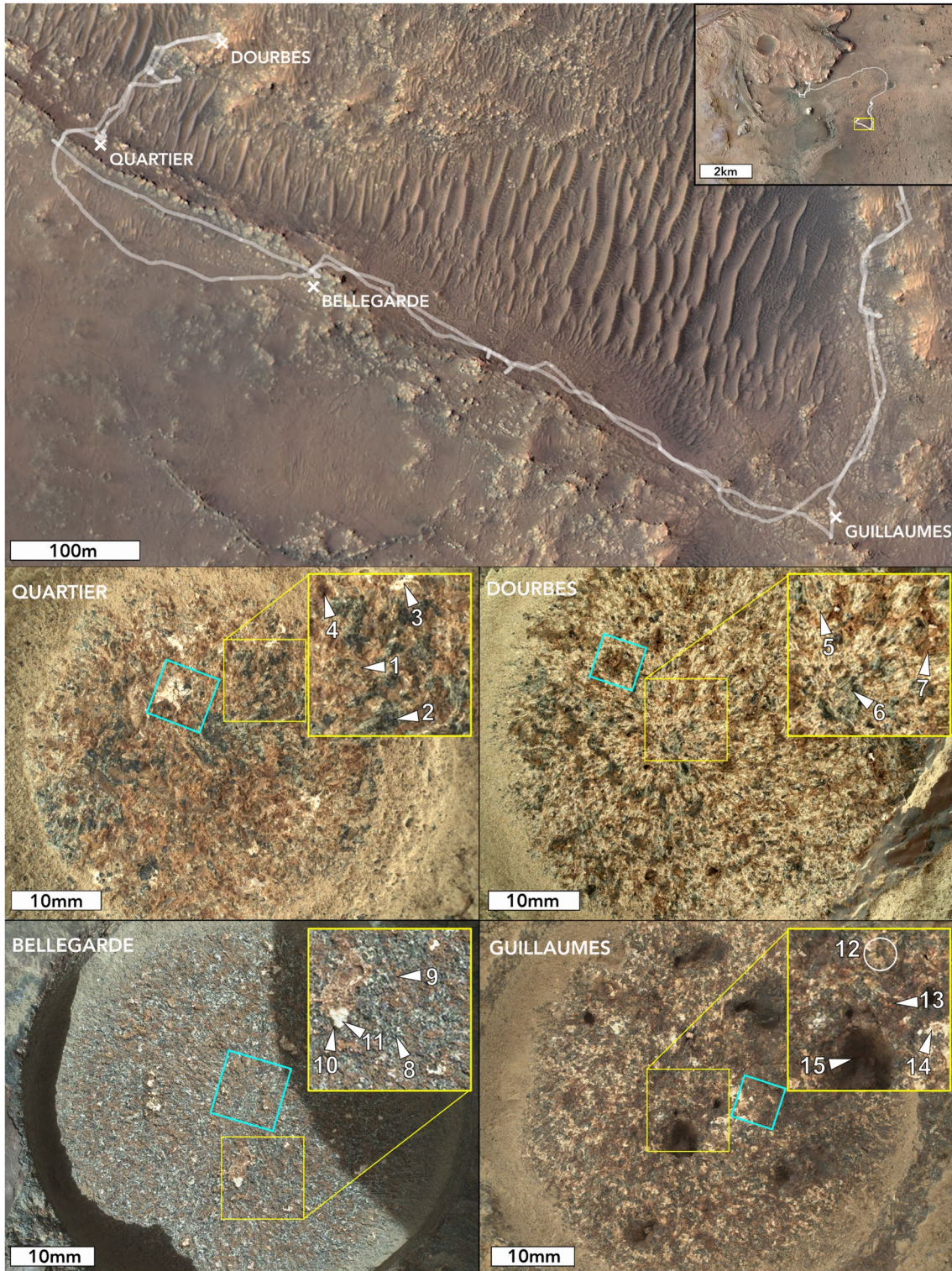
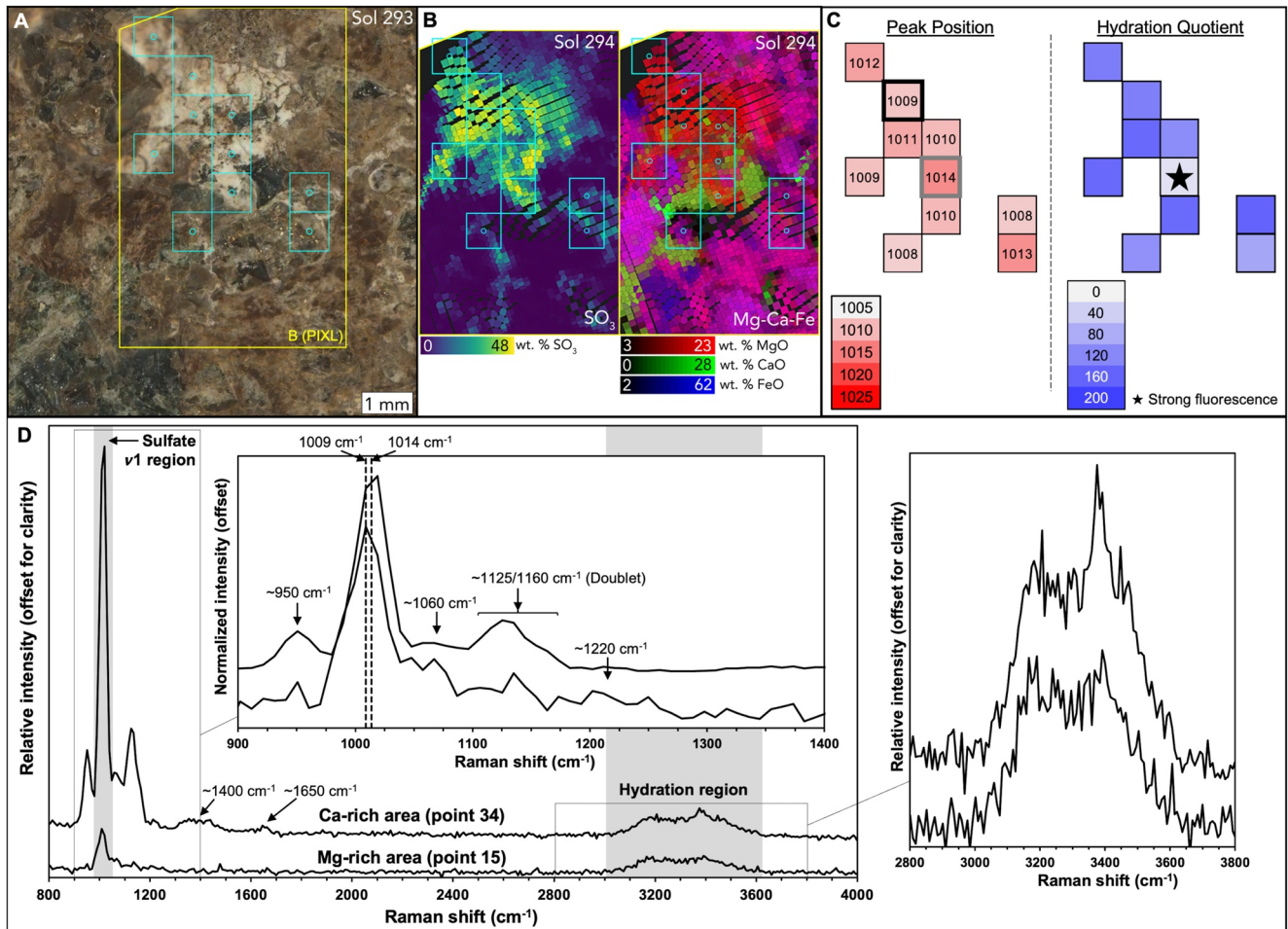


Figure 1.

scans. See Table S1 in Supporting Information S1 for a listing of all parameters used for the scans discussed in this work, and Corpolongo et al. (2023) for a full listing of parameters used during the Crater Floor Campaign. Both scan types include 100 analysis points in a 10 × 10 grid. The HDRs enable 7 × 7 mm “large area” scans to assess the diversity within an analysis area and, since the distance between steps is 780 μm, are typically used





**Figure 2.** Scanning Habitable Environments with Raman and Luminescence for Organics and Chemistry (SHERLOC) and Planetary Instrument for X-ray Lithochemistry (PIXL) sulfate mineral compositions from the Quartier abrasion (SHERLOC sol 293). (a) Colorized ACI image of the analyzed region. The cyan boxes indicate the SHERLOC scan points where sulfate phases were detected at  $\text{SNR} \geq 10$ . Cyan circles within each box indicate the position and size of the SHERLOC laser spot. The yellow polygon indicates the area of the PIXL scan on sol 294. (b) PIXL maps of  $\text{SO}_3$  abundance (left) and  $\text{MgO}$ ,  $\text{CaO}$ , and  $\text{FeO}$  abundances (right). (c) Heat maps of sulfate  $\nu_1$  peak positions and of hydration quotients (HQ, see text for how this was calculated). The heat maps for all abrasions have the same color scale (cf. Figures 3–6). The analysis spot with a fluorescence signal is indicated by a black star in the HQ map (the solid star indicates high fluorescence  $>5,000$  counts). (d) Representative SHERLOC Raman spectra from Ca-, and Mg-rich areas in the PIXL elemental map. Points 15 and 34 are indicated by the bold black and gray outlines, respectively, in panel (c). The regions where sulfate  $\nu_1$  and hydration features can be found are indicated by gray shading. Insets show details of the main sulfate peaks of each spectrum, which have here been normalized to the same sulfate  $\nu_1$  peak height for ease of comparison, and of the hydration bands, which are not normalized. The vertical dashed lines indicate the fitted center for the  $\nu_1$  peak of each spectrum. Other important peak centers are indicated.

when grain sizes are  $>1$  mm. HDR scans used between 100 and 500 pulses per point. The Detail scans are each  $1 \times 1$  mm in area with  $100 \mu\text{m}$  steps between points giving full coverage over a smaller area than the HDR scans. All Detail scans used 500 pulses per point. A third operational mode is a Survey scan. These include 1,296

**Figure 1.** Locations from the Crater Floor Campaign where sulfate phases were detected by Scanning Habitable Environments with Raman and Luminescence for Organics and Chemistry (SHERLOC). Upper panel: map of the southern portion of the Crater Floor Campaign traverse (white track) and four abrasion targets (each marked with an “x”), two within the Séítah formation (Quartier and Dourbes) and two within the Mááz Formation (Bellegarde and Guillaumes). The inset in the upper right corner shows the regional context within Jezero crater. Lower panels: WATSON images of the four sulfate mineral-bearing abrasions of the Crater Floor Campaign. The yellow squares in each panel correspond to insets showing details described in the text. Quartier panel: (1) tan olivine grain; (2) gray-green possible pyroxene grain; (3) white alteration material (sulfate phases); (4) red-brown staining. Dourbes panel: (5) tan olivine grain; (6) gray-green pyroxene grain; (7) white-brown alteration material (including sulfate phases). Bellegarde panel: (8) sub-millimeter-scale pyroxene and plagioclase; (9) red-brown staining; (10) brown isopachous void-filling cement; (11) white void-filling phase. Guillaumes panel: (12) light and dark interlocking grains; (13) red-brown staining; (14) white alteration phases; and (15) secondary voids. The cyan squares in each panel show the regions from which SHERLOC scans were performed (see Figures 2–6). WATSON images in lower panels include SII\_0292\_0692866773\_550ECM\_N0090000SRLC00702\_0000LMJ01 (Quartier), SII\_0269\_0690819279\_328ECZ\_N0080000SRLC00062\_000095J01 (Dourbes), SII\_0185\_0683375452\_164ECZ\_N0070000SRLC00001\_000095J01 (Bellegarde), and SII\_0185\_0683375452\_164ECZ\_N0070000SRLC00001\_000095J01 (Guillaumes).

analysis points in a grid of  $36 \times 36$  analysis points. They enable analysis over a large area (5 mm) with 144  $\mu\text{m}$  spacing for nearly complete coverage, and are run at 15 pulses per point.

### 2.3. Description of PIXL (Planetary Instrument for X-Ray Lithochemistry)

The PIXL is a micro-focus X-ray fluorescence (XRF) spectrometer with a 120  $\mu\text{m}$ -diameter (at 7.5 keV) X-ray beam (Allwood et al., 2020). PIXL provides the elemental compositions of rock and regolith targets at the scale of a 10 $\times$  magnifying geological hand lens. PIXL's micro-XRF scans range in size and type, including lines, square grids, and maps of rectangular areas. For the purposes of this study, we only focus on map scans from the crater floor, which consist of  $\sim 3,000$  spatially-contiguous XRF analysis points separated by 125  $\mu\text{m}$ , with scan dimensions of up to 12.5  $\times$  4.0 mm. PIQUANT, PIXL's analytical software, converts the XRF spectra for each analysis point within the map into elemental abundances (Elam & Heirwegh, 2022; Heirwegh et al., 2022). PIXL does not directly quantify elements lighter than sodium (Allwood et al., 2020). The micro context camera (MCC) takes context images for each micro-XRF scan. The co-aligned context images and micro-XRF map scans allow for the investigation of the chemical, mineral, and textural relationships between mineral phases in the crater floor targets.

### 2.4. Data Collection and Co-Localization

During SHERLOC and PIXL operations, the instruments, which are positioned on the rover arm, were typically placed on the same area of the abrasion targets to obtain co-registered data. SHERLOC scans were performed after sunset on the sol after abrasion at LMST 19:00–23:00, when the air temperature is  $-50$  to  $-70^\circ\text{C}$  and humidity is below 2% (Polkko et al., 2023). The one exception was the scan of the Guillaumes abrasion, which was performed before sunset (at LMST 16:30–17:30) on sol 167 when humidity was below 2% and air temperature was approximately  $-32^\circ\text{C}$ . PIXL scans were performed overnight after each SHERLOC scan. In some cases, follow-up scans of SHERLOC and PIXL were performed on the same analysis area or a different area up to 10 sols later. These measurements were performed during the late martian spring to summer.

The SHERLOC and PIXL data and ACI and MCC images were visually compared to overlay the data. The difference in data acquisition including spacing of measurement points and acquisition depth has been discussed in earlier papers (e.g., Razzell Hollis et al., 2022).

### 2.5. SHERLOC Data Treatment

All SHERLOC data were initially analyzed using the software package Loupe (Uckert, 2022) to compare spectral and textural features from each scan. SHERLOC Raman spectra of sulfate minerals are dominated by internal vibrations of the  $\text{SO}_4^{2-}$  ion. The most intense Raman active vibration is the symmetric stretching  $\nu_1$  mode between  $\sim 980$  and  $1,050\text{ cm}^{-1}$  followed by the asymmetric stretching  $\nu_3$  mode between  $\sim 1,050$  and  $1,250\text{ cm}^{-1}$ . Sulfate  $\nu_2$  and  $\nu_4$  bending modes occur at  $\sim 450$ – $500$  and  $\sim 600$ – $700\text{ cm}^{-1}$ , respectively and are thus within the region of signal attenuation of the SHERLOC optics described in Section 2.2 and were not detected. In the case of solid sulfate phases, both  $\nu_1$  and  $\nu_3$  Raman peak positions show significant dependence on salt composition, stoichiometry, and crystal structure, making Raman spectroscopy a suitable tool for the identification of sulfate mineral classes and individual minerals. For example, sulfate spectra have an inverse correlation between the  $\nu_1$  peak position and degree of hydration, making it possible to identify how many waters are contained in a sulfate mineral phase (Chio et al., 2005; Culka et al., 2014; Wang, Freeman, et al., 2006). Hydrated sulfate minerals also show intense O-H stretching Raman bands between  $\sim 3,000$  and  $3,600\text{ cm}^{-1}$  and an approximately one order of magnitude less intense possible H-O-H bending band at  $\sim 1,600$ – $1,700\text{ cm}^{-1}$ . The combined O-H stretching bands combined often have a complex spectral shape that depends on sulfate crystal structure and hydration state.

The spectra included in our analyses were from the four abrasions noted above (Figure 1) and were selected from those that confidently contained sulfate minerals based on the assessment made by Corpolongo et al. (2023). These spectra were peak-fitted so that accurate comparisons of peak parameters—centers, intensities, areas, and full widths at half maximum (full width at half maximum (FWHM))—could be made. Details of the peak fitting procedure are provided in Text S1 in Supporting Information S1.

In order to confidently identify different sulfate species, it was necessary to be able to identify peak centers as accurately as possible. Thus, we chose to only analyze spectra that had a signal-to-noise (SNR) ratio of 10 or

greater for the sulfate  $\nu_1$  peak (with an exception for some data from Bellegarde, see Section 3.3). Details of the SNR determination are provided in Text S1 in Supporting Information S1.

Virtually all of the sulfate spectra from the crater floor abrasions that had sufficient  $\nu_1$  peak intensities (SNR > 10) included broad bands in the Raman region between  $\sim 3,000$  and  $3,600\text{ cm}^{-1}$  resulting from water O-H stretching. In order to compare the degree of hydration of the sulfate minerals, we calculated a “hydration quotient” (HQ) for each spectrum, defined as the ratio of the total area of the two fitted hydration bands to the fitted height of the sulfate  $\nu_1$  peak (Table 3 and Table S5).

Fluorescence intensity values (Table S5) were obtained by reading the maximum intensities of the doublet peaks at  $\sim 303$  and  $326\text{ nm}$  in the software package Loupe (Uckert, 2022) similar to what is described by Sharma et al. (2023). No prior data processing was performed.

Interpretations of the cations and hydration states of the sulfate phases here described (discussed in Section 4) are made on the basis of comparisons with data from the literature and with reference samples measured by SHERLOC analogue instruments. See Text S3 in Supporting Information S1 for details of these instruments and analytical parameters used for measuring the spectra of the reference samples.

## 2.6. PIXL Data Treatment

PIXL elemental abundances were analyzed and exported from PIXLISE (Nemere et al., 2022a, 2022b), an open-source data visualization tool made for high-density imaging and XRF spectroscopy data that utilize PIQUANT (Elam & Heirwegh, 2022; Heirwegh et al., 2022). PIXLISE enables users to toggle between panels to examine the  $\mu\text{XRF}$  spectra and visualize the quantified data in the form of ternary diagrams, binary plots, false color maps of regions of interest and enriched elemental concentrations, and more. We used the previously developed methods and expressions in PIXLISE to correct for topographic orientation and diffraction effects in the elemental abundance values (Tice et al., 2023; Wright et al., 2022).

Since PIXL cannot directly measure elements lighter than sodium, the total quantified value calculated by PIXL may add up to less than 100 wt%. To find the hydration state, we assume the difference between the total quantified value and 100 wt% can be attributed completely to  $\text{H}_2\text{O}$  molecules after removing PIXL analysis points with carbonate mineral detections (Tice et al., 2022). We then take this value and the measured  $\text{SO}_3$  value to calculate the number of  $\text{H}_2\text{O}$  molecules present (see Text S2 in Supporting Information S1 for a more detailed description of hydration calculation).

Due to the relatively large analysis volume of PIXL, a typical PIXL analysis spot will probe both a sulfate phase and surrounding mineral phases. Subsequently, to retrieve elemental quantifications for just the sulfate minerals, the portion of each element attributable to silicate and chloride (NaCl) phases were stripped from the total values measured by PIXL (Liu et al., 2022; Tice et al., 2022; see Text S2 in Supporting Information S1 for a more detailed description of mineral stripping for each target including PMC points used, sulfate phase ROI elemental abundances before stripping, and elemental abundances of silicate minerals).

## 3. Results

Here we report results of analyses of sulfate minerals in the Quartier, Dourbes, Bellegarde, and Guillaumes abrasions using data from SHERLOC and PIXL, including sulfate mineral speciation, hydration state, crystallinity, and associated fluorescence.

### 3.1. Quartier

The Quartier abrasion was performed on sol 292 followed by the first SHERLOC scan on sol 293 and the first PIXL scan on sol 294. A second set of SHERLOC scans were performed on sol 304. Between sol 294 and 304, the Issole outcrop was sampled, leading to vibration and the production of drill cuttings, both of which slightly altered the surface of the abrasion (cf. Figures 2 and 3a, Figure S1 in Supporting Information S1). SHERLOC data presented here include those from the sol 293 HDR scan and from the four sol 304 Detail scans, all performed at 500 pulses per point (see Table S1 in Supporting Information S1).

The Quartier abrasion hosts irregularly distributed millimeter-scale tan crystals with sub-angular to angular morphologies (olivine), 1–4 mm green-gray, elongate and angular crystals (pyroxene), and <0.1 mm



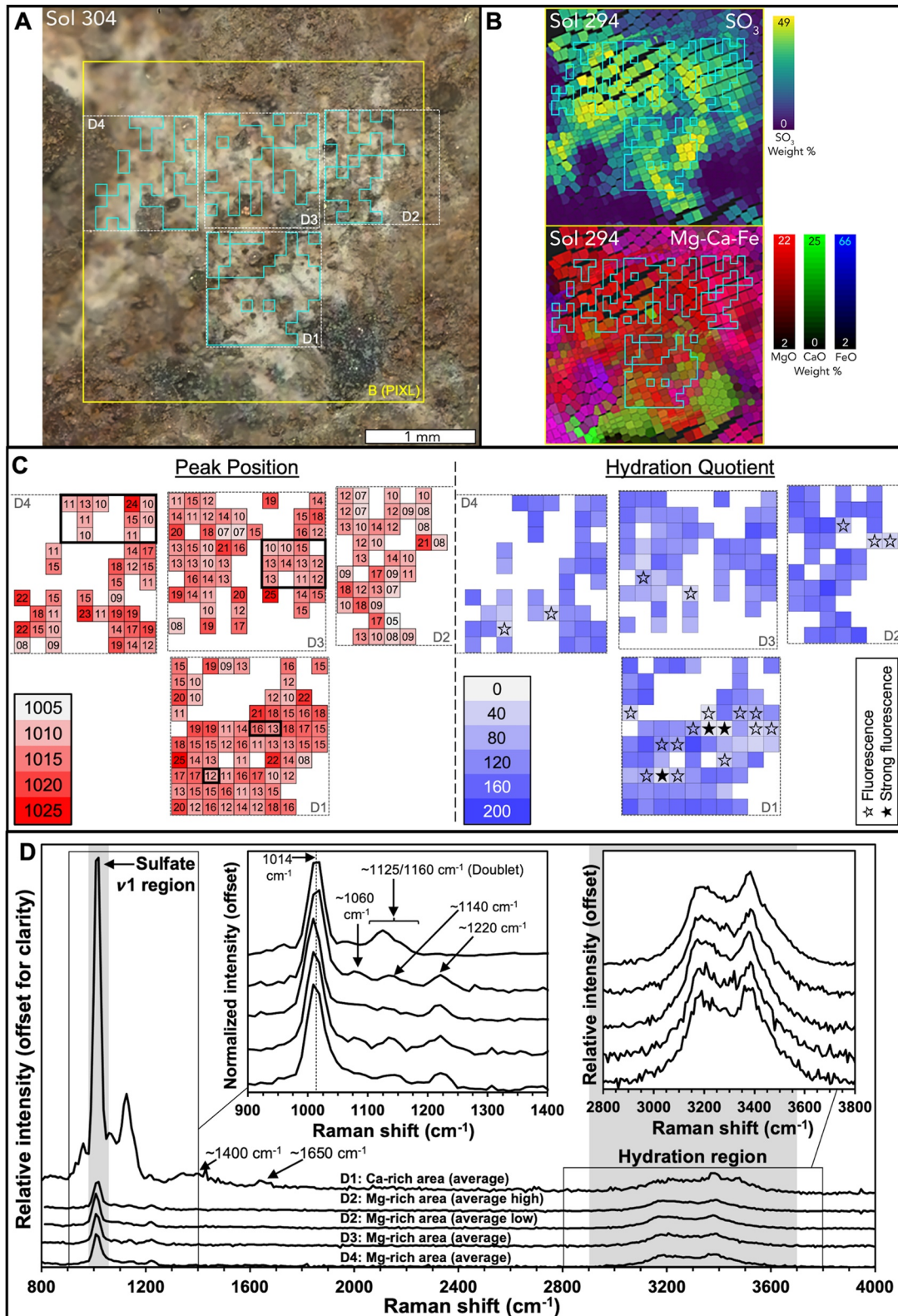


Figure 3.

**Table 1**  
*Planetary Instrument for X-Ray Lithochemistry Elemental Abundances of Sulfate Mineral Patches of Crater Floor Campaign Abrasions After Stripping Silicate Minerals and NaCl*

Oxide (wt%)	Quartier			Dourbes		Bellegarde	Guillaumes
	Mg-rich	Ca-rich	Fe-rich	Mg-rich	Fe-rich	Ca-rich	Ca-rich
Na <sub>2</sub> O	1.8 ± 1.0	2.8 ± 1.2	1.3 ± 0.9	1.4 ± 1.7	1.1 ± 1.2	1.5 ± 1.8	-1.9 <sup>a</sup> ± 1.5
MgO	16.1 ± 0.9	12.6 ± 0.7	16.6 ± 1.0	14.9 ± 1.0	19.5 ± 1.0	0.7 ± 0.6	4.7 ± 0.5
Al <sub>2</sub> O <sub>3</sub>	1.0 ± 0.3	0.8 ± 0.2	0.7 ± 0.3	0.0 ± 0.2	0.2 ± 0.2	0.3 ± 0.4	–
SO <sub>3</sub>	38.9 ± 1.6	44.8 ± 1.8	31.5 ± 1.5	27.2 ± 1.0	22.0 ± 1.0	32.5 ± 0.5	15.5 ± 0.7
CaO	1.6 ± 0.3	12.7 ± 0.5	1.0 ± 0.2	0.7 ± 0.3	2.0 ± 0.3	17.9 ± 0.7	14.0 ± 0.7
MnO	0.1 ± 0.1	0.06 ± 0.1	0.2 ± 0.2	0.4 ± 0.2	0.8 ± 0.2	0.1 ± 0.2	0.3 ± 0.2
FeO-T	1.4 ± 0.6	4.1 ± 0.5	11.0 ± 1.0	8.3 ± 0.8	21.8 ± 0.8	-0.68 <sup>a</sup> ± 2.0	0.4 ± 0.7
H <sub>2</sub> O	25.0	15.5	-	-	-	5.2	3.0
Total	85.9	93.4	62.0	53.0	68.2	57.6	36.0

<sup>a</sup>Negative values are the result of imperfect knowledge of cation compositions of phases used to remove other mineral components from sulfate mineral elemental abundances. The values are assumed to be 0 or very close. Note that the values have not been renormalized after stripping.

subrounded to subangular white crystals (Figures 1 and 2a; Wogslund et al., 2023). Light-toned material occurs along many grain boundaries and red (likely Fe) staining occurs throughout, indicative of aqueous alteration and oxidation of the primary phases (Wogslund et al., 2023). Sulfate phases are predominantly identified as large exposures of light-toned to white material (Figure 2). The sulfate mineral patch contains features similar to so-called “chicken-wire” textures (Nachon et al., 2014). This sulfate mineral patch has previously been shown to be surrounded by carbonate phases and some scattered detections of perchlorate/chlorate or phosphate phases (Corpolongo et al., 2023).

The greatest weight percentage of SO<sub>3</sub> in the Quartier abrasion is concentrated in the brightest white colored areas (Figure 2b). Based on the PIXL cation distributions, the sulfate mineral patch in Quartier can be divided into three different general areas: Mg-dominated with minor Ca and Fe, mixed Mg and Ca, and mixed Mg and Fe (Table 1 and Figures 2 and 3b). Sodium (Na) and potassium (K) are fairly evenly spread across the sulfate mineral patch at ~2 and <0.2 wt%, respectively (Table 1 and Table S3 in Supporting Information S1), indicating only minor impurities.

The Mg-dominated area (post silicate stripping, Table 1), which consists of MgO (~16 wt%) and small amounts of CaO (<2 wt%) and FeO (<2 wt%) and ~39 wt% SO<sub>3</sub>, comprises the left and upper part of the sulfate mineral patch (Figures 2 and 3b). In these areas, the fitted sulfate ν<sub>1</sub> Raman peak positions vary typically between 1,009 and 1,012 cm<sup>-1</sup> in the sol 293 scan and 1,009 and 1,015 cm<sup>-1</sup> in the sol 304 scan, although there are outliers as low as 1,007 cm<sup>-1</sup> and as high as 1,023 cm<sup>-1</sup> in the sol 304 scan (Figures 2 and 3c). When comparing scan points that are less than 500 μm from each other in the sol 293 and 304 data sets, there is a 2 cm<sup>-1</sup> peak center difference between sol 293 and 304, which is less than the uncertainty of SHERLOC measurements (see Text S1

**Figure 3.** Scanning Habitable Environments with Raman and Luminescence for Organics and Chemistry (SHERLOC) and Planetary Instrument for X-ray Lithochemistry (PIXL) sulfate mineral compositions from the Quartier abrasion (SHERLOC sol 304). (a) Colorized ACI image of the analyzed region. The light gray boxes indicate the four detailed scans (labeled D1–4) analyzed by SHERLOC on sol 304 (compared with Figure 2). The cyan boxes indicate the SHERLOC scan points where sulfate phases were detected at SNR ≥ 10. The laser spots are annuli that fit within the squares. The yellow square indicates the area of the PIXL scan on sol 294. (d) PIXL maps of SO<sub>3</sub> abundance (top) and MgO, CaO, and FeO abundances (bottom). The data are the same as those shown in Figure 2. (c) Heat maps of sulfate ν<sub>1</sub> peak positions and of hydration quotients (HQ, see text for how this was calculated). Note that for the peak positions, to increase the legibility of the labels, only the last two digits are given. The first two digits for each are “10.” The heat maps for all abrasions have the same color scale (cf. Figures 2, 4–6). Analysis spots with fluorescence are indicated by black stars in the HQ maps (solid stars indicate high fluorescence >5,000 counts). (d) Representative SHERLOC Raman spectra from Ca- and Mg-rich areas in PIXL elemental maps. The points from which the averaged spectra come for D1, D3, and D4 are indicated by bold black outlines in panel (c). The points from which the averaged spectra come for the D2 scan are those with peak centers between 1,005 and 1,010 cm<sup>-1</sup> (“low”) and between 1,011 and 1,025 cm<sup>-1</sup> (“high”). Compare with Table 3. The regions where sulfate ν<sub>1</sub> and hydration Raman features can be found are indicated by gray shading. Insets show details of the main sulfate peaks of each spectrum, which have here been normalized to the same sulfate ν<sub>1</sub> peak height for ease of comparison, and of the hydration bands, which are not normalized. Important peak centers are indicated. The dashed vertical line centered at 1,014 cm<sup>-1</sup> indicates the peak center of the D1 Ca-sulfate peak and is similar to the center of the ν<sub>1</sub> peak of the other spectra.

**Table 2**  
SHERLOC Sulfate  $\nu 1$  Peak Positions and Hydration Quotients on Mission Sols 293 and 304

Sol 293 points	Sol 304 scan and points	Distance apart (mm)	Peak center sol 293 ( $\text{cm}^{-1}$ )	Peak center sol 304 ( $\text{cm}^{-1}$ )	HQ sol 293	HQ sol 304
34	Detail 1, 45	0.04	1,014	1,016	20	16
45	Detail 1, 94	0.26	1,010	1,012	153	156
45	Detail 4, 90	0.44	1,010	1,012	153	155
24	Detail 1, 0	0.45	1,011	1,015	155	162

in Supporting Information S1) and can thus be considered indistinguishable from each other (Table 2). The spectra from these areas are dominated by a strong  $\nu 1$  peak, a clear peak at  $\sim 1,220 \text{ cm}^{-1}$ , and several smaller peaks between these two that form a mostly unresolvable slope. This slope is likely formed by  $\nu 3$  peaks with a possible contribution from the carbonate  $\nu 1$  peak ( $\sim 1,085 \text{ cm}^{-1}$ ), although this is likely minor because of low Fe values in this area. In some spectra, peaks at  $\sim 1,080$  and  $\sim 1,150 \text{ cm}^{-1}$  can be distinguished in the slope. The O-H stretching modes form a doublet with peak centers around  $\sim 3,200$  and  $\sim 3,400 \text{ cm}^{-1}$  and are very similar between sol 293 and 304 data (Figures 2d and 3d and Figure S1 in Supporting Information S1). The HQ (see Section 2.5 for a definition) values in Quartier are generally high ( $>80$ ). Assuming no carbonate phases in this part of the sulfate mineral patch and using the totals and  $\text{SO}_3$  concentration before mineral stripping indicates a hydration state for sulfate minerals of around three waters in this part of the sulfate mineral patch (Table 1).

Regions of mixed Mg and Fe consist of  $\sim 17 \text{ wt\% MgO}$  and  $\sim 11 \text{ wt\% FeO}$  and are mostly found in the right part of the sulfate mineral patch (Figures 2 and 3). They contain  $\sim 1 \text{ wt\% CaO}$  and  $\sim 30 \text{ wt\% SO}_3$ . In this area, the sulfate  $\nu 1$  peak positions vary between  $1,005$  and  $1,017 \text{ cm}^{-1}$  with outliers as high as  $1,020 \text{ cm}^{-1}$  in the sol 304 scans (Figure 3). SHERLOC sulfate spectra from this region obtained on sol 293 were relatively weak ( $\text{SNR} < 10$ ) and are not considered further. The spectra resemble those obtained in the Mg-dominated area, with a major  $\nu 1$  peak and a sloping shoulder composed of largely unresolvable peaks between  $1,040$  and  $1,200 \text{ cm}^{-1}$  from  $\nu 3$  peaks and a clear peak at  $1,220 \text{ cm}^{-1}$  (Figure 3). The HQ values in this area are also similar to that of the Mg-dominated area ( $>80$ ) (Figures 2 and 3c). Because of the likely presence of carbonate phases and topography in this area, it is difficult to estimate the number of stoichiometric waters from the PIXL data.

Regions of mixed Mg and Ca have similar MgO contents as the mixed Mg and Fe regions ( $\sim 13 \text{ wt\%}$ ) but a larger concentration of CaO ( $\sim 13 \text{ wt\%}$ ) and lower amounts of FeO ( $\sim 4 \text{ wt\%}$ ). These regions are found primarily in the right and lower part of the sulfate mineral patch (Figures 2 and 3b). Some of the highest concentrations of sulfur are found in this area ( $\sim 45 \text{ wt\%}$ ). Raman spectra from this area contain sulfate  $\nu 1$  peaks with centers of  $1,013$ – $1,020 \text{ cm}^{-1}$  and a double  $\nu 3$  peak at  $1,125$  and  $1,160 \text{ cm}^{-1}$  (Figures 2d and 3d). The HQ values are generally low in this area ( $<80$ ), indicating limited hydration compared to the mixed Mg and Fe regions. The shape of the hydration doublet is similar to that of those in areas of high Mg content except one point (point 45) in the sol 304 data, where the peak at  $\sim 3,200 \text{ cm}^{-1}$  is significantly less intense than the other points (Figure 8 and Figure S1 in Supporting Information S1). Assuming no carbonate phases in this area and taking the PIXL totals and  $\text{SO}_3$  indicates a hydration state for sulfate minerals of  $\sim 1.5$  water in this area (Table 1). The three most intense sulfate spectra from this area also contain additional peaks at  $\sim 1,380$  and  $\sim 1,650 \text{ cm}^{-1}$  (Figures 2d and 3d). One additional point only contains a band at  $\sim 1,380 \text{ cm}^{-1}$ .

### 3.2. Dourbes

The Dourbes abrasion was performed on sol 253, the SHERLOC scan on sol 269, and the PIXL scan on sol 270. The SHERLOC data presented here include the sol 269 Detail 1 scan using 500 pulses per point (see Table S1 in Supporting Information S1).

The Dourbes abrasion is dominated by millimeter-scale tan and light gray/green minerals (olivine and pyroxene, respectively), with medium brown colored material occurring along grain edges/boundaries (Figures 1 and 4a; Wogsland et al., 2023). Co-registered SHERLOC and PIXL analyses reveal a poikilitic texture for Dourbes that contains olivine engulfed by pyroxene (Liu et al., 2022) along with minor amounts of carbonate, sulfate, and perchlorate phases, and possible feldspar. The sulfate phases are found in whitish/brown patches. Similar to the Quartier abrasion, the sulfate phases in Dourbes are surrounded by a rim of carbonate phases (Corpolongo et al., 2023). One detection of a perchlorate/phosphate phase associated with sulfate phases has also been noted (Corpolongo et al., 2023).

SHERLOC and PIXL data reveal differences between sulfate phases in the Dourbes and Quartier abrasions (Table 1 and Figure 4). Based on the PIXL cation distributions, the sulfate mineral patch in Dourbes can be



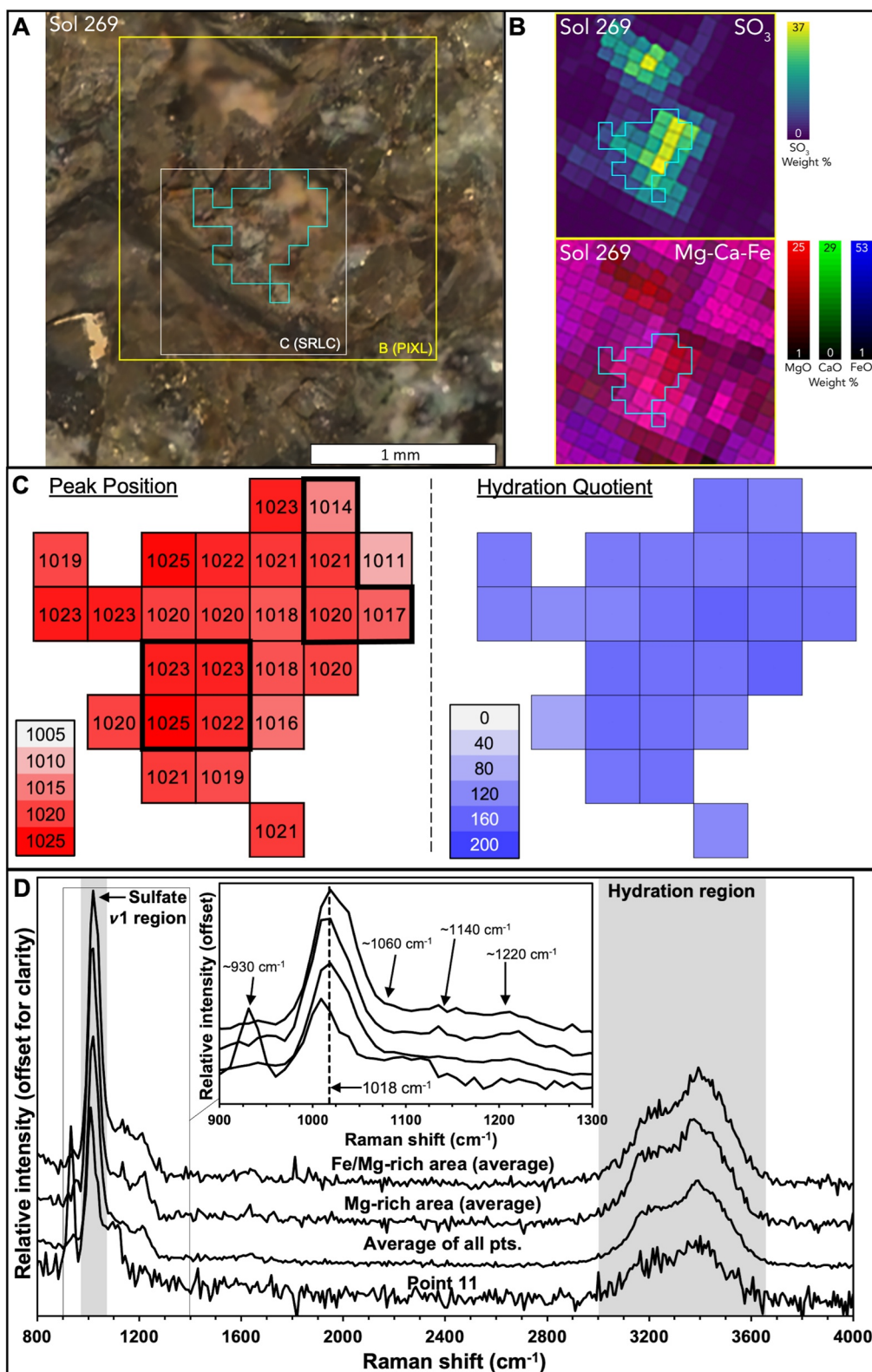


Figure 4.

divided into two areas: one has more MgO (~15 wt%) and less FeO (~8 wt%), and the other has a subequal mix of MgO (~20 wt%) and FeO (~22 wt%) (Table 1). The SO<sub>3</sub> concentration is ~25 wt%, the NaO concentration is <2 wt%, and the K<sub>2</sub>O concentration is <0.2 wt% (Table 2 and Table S3 in Supporting Information S1). SHERLOC sulfate ν1 peak centers vary between 1,017 and 1,025 cm<sup>-1</sup> with a few outliers as low as 1,011 cm<sup>-1</sup> and somewhat lower values in more Mg-rich areas (Figure 4d). Similar to those of Quartier, the sulfate ν3 peaks have a slope of unresolved smaller peaks between 1,050 and 1,200 cm<sup>-1</sup> and one clear peak at ~1,220 cm<sup>-1</sup>. Small peaks can be identified at ~1,080 and ~1,140–1,150 cm<sup>-1</sup>. The hydration peaks are centered around 3,200 and 3,400 cm<sup>-1</sup> (Table 3). Peaks in Dourbes are distinct from other targets in several ways. The fitted ν1 peak positions generally occur at higher wavenumbers and the FWHM values are larger (around 50 cm<sup>-1</sup> compared to 30–40 cm<sup>-1</sup> for other targets; Table 3). The HQ values are generally high in this target (>100) indicating more hydration, whereas the ratio between the intensities (I) of the two hydration peaks ( $I_{3,400\text{ cm}^{-1}}/I_{3,200\text{ cm}^{-1}}$ ) is higher than for the other targets (Figure 8c). Due to the presence of carbonate phases and topography in this area, it is difficult to estimate the number of stoichiometric waters in sulfate minerals from PIXL data.

### 3.3. Bellegarde

The Bellegarde abrasion was performed on sol 185, the SHERLOC scan on sol 186, and the PIXL scan on sol 187. The SHERLOC data presented here include the sol 186 HDR 1 and 2 scans run at 250 pulses per point and, because of the relatively low intensity of those spectra, HDR points and three survey scan points with an SNR greater than 5 are also presented (see Table S1 in Supporting Information S1).

The Bellegarde abrasion is consistent in composition and texture with aphanitic holocrystalline basalt (or microgabbro) (Farley et al., 2022; Schmidt et al., 2022). It is dominated by sub-millimeter-scale pyroxene and plagioclase crystals with extensive red-brown Fe-rich patches overlying both (Figures 1 and 5a), the latter likely suggesting extensive aqueous alteration. An igneous origin is suggested by an interlocking crystal texture and a lack of fine-grained matrix and intergranular cement. White (Ca-sulfate) and brown (high Fe phase) materials exhibit patchy textures and are interpreted as secondary minerals (Scheller et al., 2022; Woglsland et al., 2023). In some instances, the white material is in direct contact with dark matrix minerals and in other instances, it is surrounded by brown material (Figures 1 and 5a). Petrographic analyses indicate that the brown material formed isopachous cement within secondary voids, which were later filled by the white material (Woglsland et al., 2023). Tentative mineral identifications within this area include carbonate, sulfate, phosphate, and silicate minerals (Copolongo et al., 2023), though secondary mineralization seems less extensive than other abrasions such as Guillaumes.

PIXL analyses of the white patch in the upper left corner reveal that it has a major cation composition of CaO ~18 wt%, MgO ~1 wt%, and FeO ~0 wt% and the SO<sub>3</sub> concentration is ~32 wt%. The minor cations include NaO (~3 wt%) and K<sub>2</sub>O (<0.5 wt%) (Table 1, Figure 5b).

The fitted sulfate ν1 peaks have a range of 1,008–1,017 cm<sup>-1</sup> (Table 3, Figure 5c). Because of the weak Raman signals, it is difficult to discern any ν3 peaks. However, PIXL data from the crescent-shaped sulfate mineral patch in the upper left corner (Figure 5a), indicate the presence of Ca-sulfate phases in the one co-localized HDR point and the three survey spectra. The other points are less clear as either they fall outside the PIXL scan area or are not clearly associated with either Mg or Ca. The SHERLOC HDR spectra show no indication of hydration and those of the survey scan are equivocal (Figure 5d). One of the three survey spectra contains a possible weak hydration feature, but the other two do not. Furthermore, the hydration calculation from PIXL indicates a hydration state

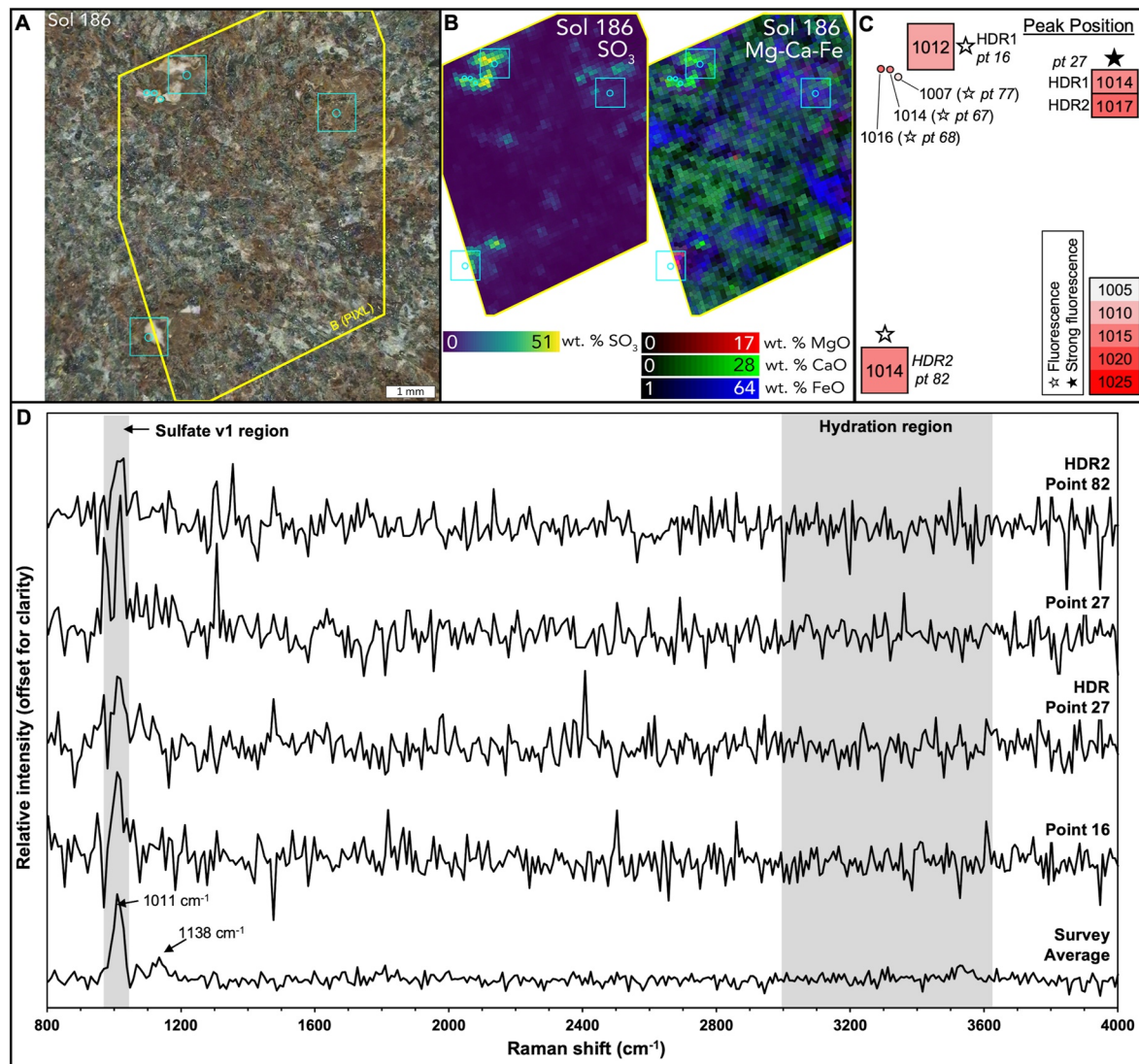
**Figure 4.** Scanning Habitable Environments with Raman and Luminescence for Organics and Chemistry (SHERLOC) and Planetary Instrument for X-ray Lithochemistry (PIXL) sulfate mineral compositions from the Dourbes abrasion. (a) Colorized ACI image of the analyzed region. The light gray box indicates the region analyzed by SHERLOC on sol 269. The cyan boxes indicate the SHERLOC scan points where sulfate phases were detected at SNR ≥10. The laser spots are annuli that fit within the cyan boxes. The yellow square indicates the area of the PIXL scan on sol 269. (b) PIXL maps of SO<sub>3</sub> abundance (top) and MgO, CaO, and FeO abundances (bottom). (c) Heat maps of sulfate ν1 peak positions and of hydration quotients (see text for how this was calculated). The heat maps for all abrasions have the same color scale (cf. Figures 2–3, 5–6). (d) Average SHERLOC Raman spectra as examples of Mg-sulfate minerals. The upper spectrum is from the lower left region (bold square of points in panel c). The second spectrum is from the upper right region (bold L-shape of data points in panel c). The third spectrum is the average of all data points. The fourth has the lowest sulfate ν1 peak center of the Dourbes data (1,011 cm<sup>-1</sup>). The regions where sulfate ν1 and hydration features can be found are indicated by gray shading. The inset shows details of the main sulfate peaks of each spectrum, which have here been normalized to the same sulfate ν1 peak height. Important peak centers are indicated. The dashed vertical line centered at 1,018 cm<sup>-1</sup> indicates the peak center of the third spectrum.

**Table 3**  
Selected Fitted Peak Parameters<sup>a</sup> of the SHERLOC Spectra in Figures 2–8

Target	Spectrum	Sulfate $\nu 1$ mode			Hydration O-H stretch 1			Hydration O-H stretch 2			Hydration quotient (HQ) <sup>b</sup>	Figure reference
		Center (cm <sup>-1</sup> ) <sup>c</sup>	Peak height	FWHM	Center (cm <sup>-1</sup> )	Peak height	Area	Center (cm <sup>-1</sup> )	Peak height	Area		
Quartier												
Sol 293	Ca-sulfate (point 34)	1,014	11,745	32	3,174	421	63,414	3,389	618	170,307	20	2D
Sol 293	Mg-sulfate (point 15)	1,009	1,149	37	3,191	420	62,544	3,392	445	86,962	130	2D
Sol 304 Detail 1	Ca-sulfate (average of points 45, 46, and 77)	1,014	9,744	30	3,179	250	55,058	3,408	433	119,472	18	3D, 8A
Sol 304 Detail 2	Mg-sulfate (avg. of sulfate $\nu 1$ peaks >1,010 cm <sup>-1</sup> )	1,014	695	31	3,182	225	42,516	3,376	255	65,406	155	3D
Sol 304 Detail 2	Mg-sulfate (avg. of sulfate $\nu 1$ peaks $\leq$ 1,010 cm <sup>-1</sup> )	1,009	822	31	3,176	263	47,328	3,369	295	73,558	147	3D
Sol 304 Detail 3	Mg-sulfate (avg. of pts 32, 33, 46, 47, 48, 49, 50, 51, 53)	1,012	818	32	3,186	229	51,253	3,377	267	75,611	155	3D
Sol 304 Detail 4	Mg-sulfate (avg. of pts 4, 5, 6, 8, 9, 10, 11, 14, 25, 28)	1,012	729	29	3,190	257	57,972	3,391	272	65,608	169	3D,8B
Dourbes												
Detail 1	Fe-Mg-rich area (avg. of pts 33, 34, 44, 45)	1,022	1,626	51	3,270	423	146,171	3,447	417	88,568	144	4D
Detail 1	Mg-rich area (avg. of pts. 7, 12, 27, 28)	1,018	1,555	51	3,217	399	108,167	3,427	519	117,180	145	4D
Detail 1	Average of all sulfate points	1,018	1,169	47	3,191	290	75,283	3,410	450	113,619	162	4D,8B
Detail 1	Perchlorate-rich (point 11)	1,011	915	48	3,198	220	53,795	3,412	325	70,431	136	4D
Bellegarde												
HDR 1	Point 16	1,012	266	24	–	–	–	–	–	–	–	5D
HDR 1	Point 27	1,014	180	42	–	–	–	–	–	–	–	5D
HDR 2	Point 27	1,017	377	20	–	–	–	–	–	–	–	5D
HDR 2	Point 82	1,014	190	29	–	–	–	–	–	–	–	5D
Survey	Ca-sulfate (avg. of pts 67, 68, 77)	1,011	222	37	–	–	–	–	–	–	–	5D
Guillaumes												
HDR 1	Point 1	1,013	517	38	3,193	116	27,548	3,436	141	30,476	112	6D
HDR 1	Point 14	1,015	386	48	3,180	124	22,357	3,409	135	31,890	141	6D
HDR 1	Point 21	1,014	315	28	–	–	–	–	–	–	–	6D
HDR 1	Point 66	1,014	683	29	3,257	54	3,728	3,515	55	10,499	21	6D
Reference samples <sup>d</sup>												
	Epsomite	978	1,130	25	3,336	626	222,194	3,458	171	21,187	215	8B
	Starkeyite	997	1,443	26	3,411	329	22,156	3,413	584	181,923	141	8B
	Kieserite	1,041	369	31	3,173	58	3,592	3,271	56	22,932	72	8B
	Amorphous Mg-sulfate	1,021	349	54	3,286	40	16,992	3,453	11	2,165	55	8B
	Anhydrous Mg-sulfate	1,012	598	33	3,352	5	2,101	3,468	3	568	4	8B
	Gypsum	1,009	1,586	42	3,411	1,110	124,833	3,500	1,264	112,084	149	8A
	Anhydrite	1,017	1,127	29	3,559	30	1,023	3,590	16	2,056	3	8A

<sup>a</sup>See Supporting Table S5 for all fitted peak parameters for all sulfate spectra. <sup>b</sup>HQ is defined as the sum of the areas of hydration peaks 1 and 2 divided by the height of the sulfate  $\nu 1$  peak. <sup>c</sup>Peak position errors are  $\pm 2$  cm<sup>-1</sup> (see Section 2.5 for rationale). <sup>d</sup>See Text S3 in Supporting Information S1 for details of the reference samples (J. V. Clark et al., 2023) except for gypsum. For gypsum, see Razzell Hollis et al., 2021.





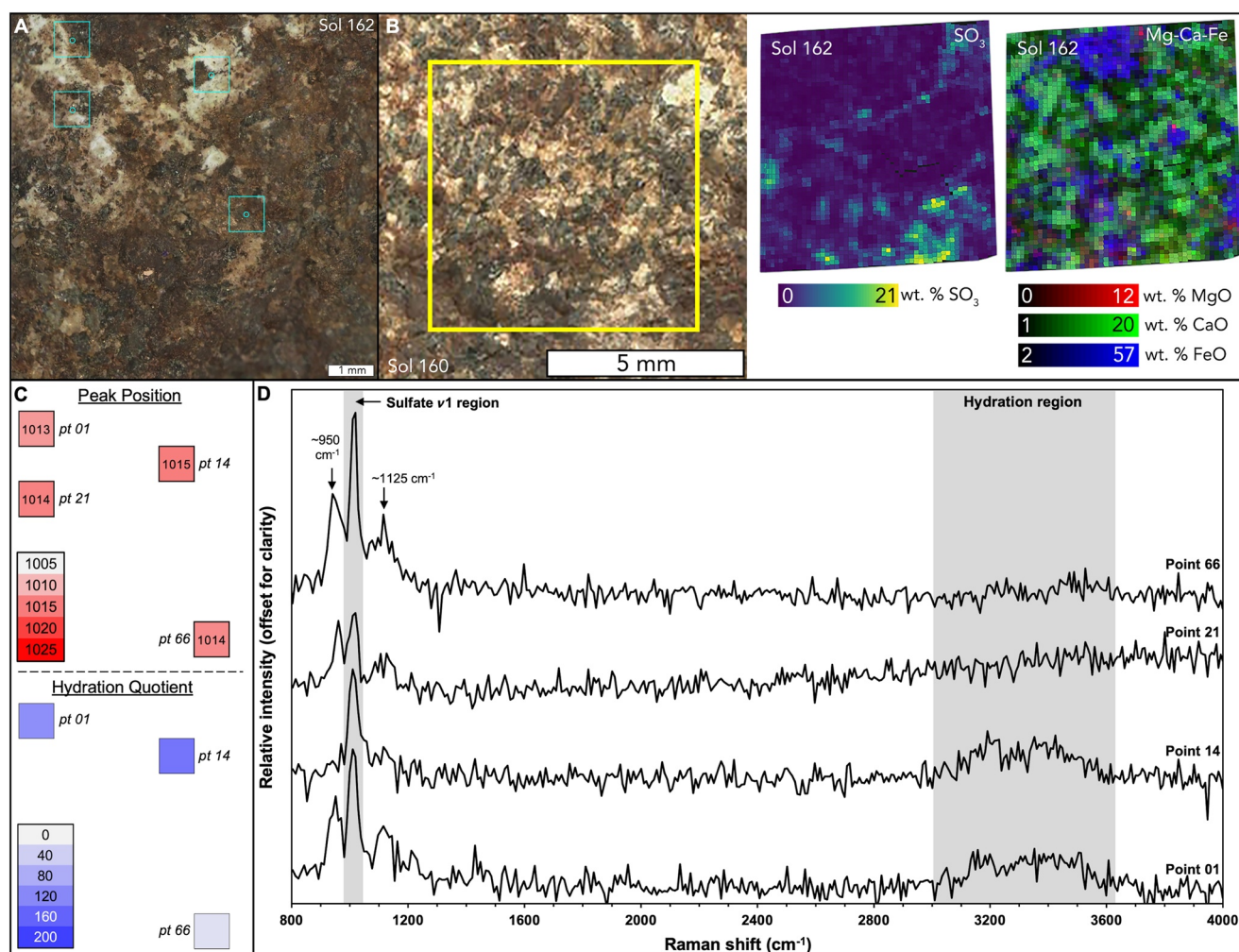
**Figure 5.** Scanning Habitable Environments with Raman and Luminescence for Organics and Chemistry (SHERLOC) and Planetary Instrument for X-ray Lithochemistry (PIXL) sulfate mineral compositions from the Bellegarde abrasion. (a) Colorized ACI image of the analyzed region. SHERLOC analyzed the entire region of this image on sol 186. The cyan boxes indicate the SHERLOC High Dynamic Range (HDR) scan points where sulfate phases were detected at  $\text{SNR} \geq 5$ . The laser spots are represented by the small cyan circles within the squares. The individual cyan circles indicate the location of the survey scan points where sulfate phases were detected at  $\text{SNR} \geq 5$ . The yellow polygon indicates the area of the PIXL scan on sol 186. (b) PIXL maps of  $\text{SO}_3$  abundance (left) and MgO, CaO, and FeO abundances (right). (c) Heat map of sulfate  $\nu_1$  peak positions. Analysis spots with fluorescence are indicated by stars (solid stars indicate high fluorescence  $>5,000$  counts). The heat maps for all abrasions have the same color scale (cf. Figures 2–4, 6<sup>2–4</sup>). (d) All four SHERLOC Raman spectra of sulfate phases from the HDR scans and the average spectrum of three points from the survey scan (points, 67, 68, and 77). Note that two scans (HDR1 and HDR2) were performed on the same spots. The regions where sulfate  $\nu_1$  and hydration features could be found are indicated by gray shading (note the absence of any hydration bands).

for sulfate minerals of less than one water in this area (Table 1). The lack of hydration even in summed spectra as noted in earlier papers is consistent with an anhydrous Ca-sulfate phase (Razzell Hollis et al., 2022).

### 3.4. Guillaumes

The Guillaumes abrasion was performed on sol 160, and SHERLOC scans on sols 161 and 162. PIXL was performed on sol 167. The SHERLOC data presented here include the sol 162 HDR1 scan using 250 pulses per point (see Supporting Table S1 in Supporting Information S1).

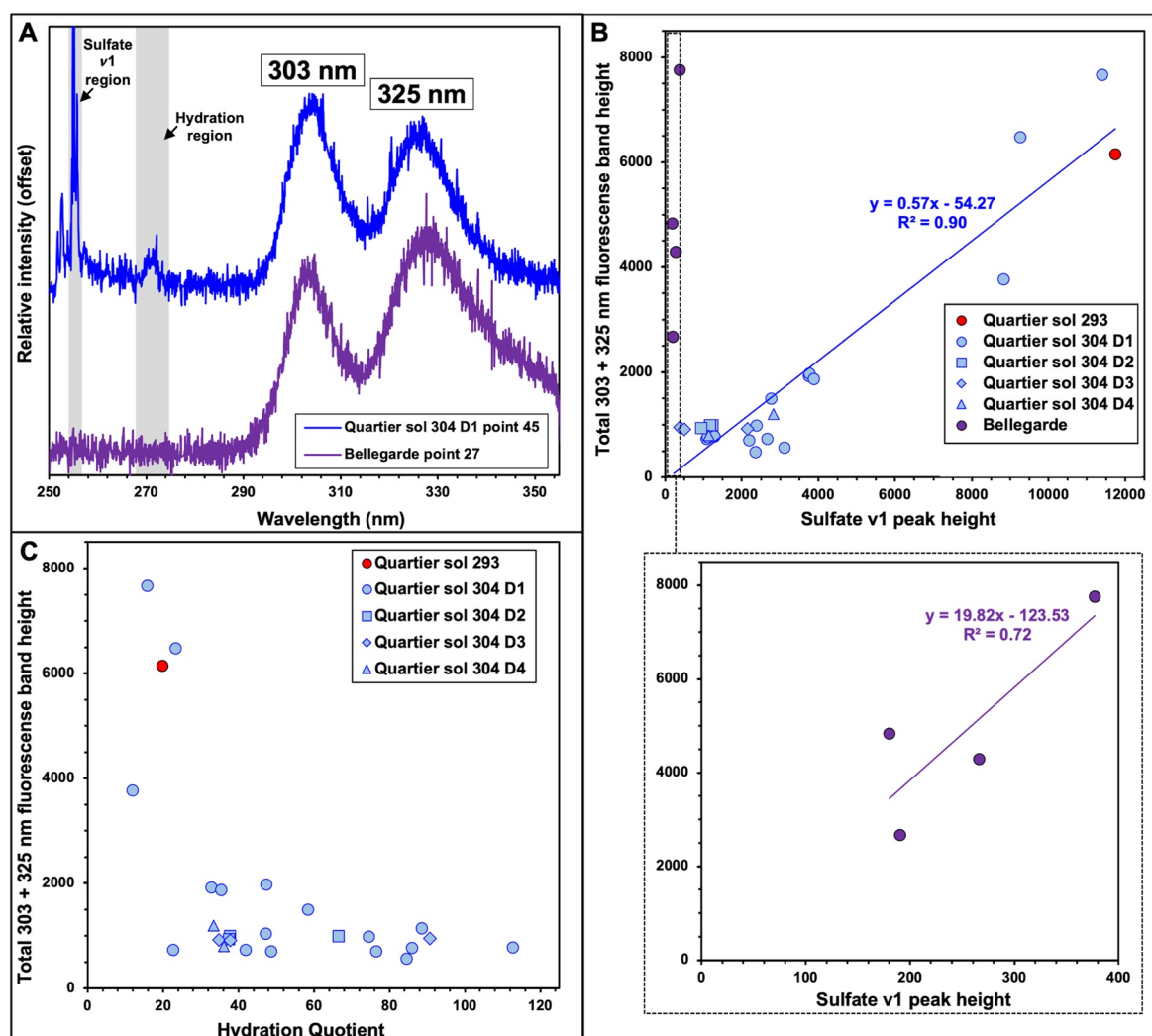
Within the broader Guillaumes abrasion, light and dark colored millimeter to sub-millimeter grains appear to be spatially homogeneous (Figures 1 and 6a). An observance of potential interlocking grains/crystals suggests that



**Figure 6.** Scanning Habitable Environments with Raman and Luminescence for Organics and Chemistry (SHERLOC) and Planetary Instrument for X-ray Lithochemistry (PIXL) sulfate mineral compositions from the Guillaumes abrasion. (a) Colorized ACI image of the analyzed region. SHERLOC analyzed the entire region of this image on sol 162. The cyan boxes indicate the SHERLOC scan points where sulfate phases were detected at  $\text{SNR} \geq 10$ . The laser spots are represented by the small cyan circles within the squares. (b) Colorized ACI image of the region of the Guillaumes abrasion where PIXL maps were acquired on sol 160 (yellow square). Note that the SHERLOC and PIXL scans were located in different regions of the abrasion. On the right side are PIXL maps of  $\text{SO}_3$  abundance (left) and MgO, CaO, and FeO abundances (right). (c) Heat maps of sulfate  $\nu_1$  peak positions and of hydration quotients (HQ, see text for how this was calculated). The heat maps for all abrasions have the same color scale (cf. Figures 2–5). (d) SHERLOC Raman spectra of sulfate phases. The regions where sulfate  $\nu_1$  and hydration features can be found are indicated by gray shading. Important peak centers are indicated.

it may be a fine-grained gabbro or holocrystalline basalt (Schmidt et al., 2022). Red-brown coloring is heterogeneously interspersed throughout (Figure 1), which is hypothesized to be Fe-oxide staining and an indication of potential aqueous alteration and secondary mineralization (Wogsland et al., 2023). White material, identified to largely consist of perchlorate and Na-perchlorate phases (Copolongo et al., 2023; Scheller et al., 2022), occurs throughout. Sulfate mineral detections within the Guillaumes abrasion occur at boundaries between white colored material and dark colored material, interfaces between white colored material with medium brown material and dark colored material, and on dark colored grains. This abrasion has a pitted appearance and is friable in nature (Figure 1).

This target does not have any directly co-registered SHERLOC and PIXL data. However, a PIXL scan performed near the SHERLOC scan area contained mostly Ca-sulfate minerals with minor Mg-sulfate minerals based on the correlation of  $\text{SO}_3$  and Mg/Ca overlap (Figures 6b and Table 1). Based on PIXL  $\text{SO}_3$  and totals (Table 1), the Ca-sulfate phases show minimal hydration ( $<1$  water). Due to only small Mg-sulfate phase areas in the PIXL scan



**Figure 7.** Comparison of total fluorescence intensity with fitted sulfate peak parameters. (a) Full Scanning Habitable Environments with Raman and Luminescence for Organics and Chemistry (SHERLOC) spectra acquired for Quartier sol 304 Detail 1 Point 45 and Bellegarde High Dynamic Range 2 Point 27 showing broad fluorescent features centered at 303 and 325 nm (cosmic rays removed). (b) The upper panel shows sulfate  $\nu_1$  Raman peak intensity versus summed intensity of both fluorescence bands for Quartier scans (blue and red symbols) and Bellegarde (purple symbols). The trendline is a linear fit through all of the Quartier data. The lower panel in B is an enlargement of the Bellegarde data (dashed boxed region in the upper panel) to show the difference in scale. The trendline is a linear fit. (c) Hydration Quotient versus summed intensity of both fluorescence bands for Quartier scans.

it is difficult to make accurate hydration calculations. However, hydration does appear higher in more Mg-rich sulfate phase areas than in Ca-sulfate phase areas.

The SHERLOC Raman spectra for Guillaumes contain peaks between 1,013 and 1,015  $\text{cm}^{-1}$  (Table 3 and Figure 6). It is difficult to distinguish sulfate  $\nu_3$  peaks in these spectra due to relatively weak signals and overlap with perchlorate  $\nu_3$  peaks (see Figure 6d). Two of the scan points have high HQ values (>80), whereas one has a low value (<80). One of the points had no detectable hydration. This indicates a mix of hydrated Mg-sulfate and anhydrous Ca-sulfate in Guillaumes.

### 3.5. Fluorescence

A fluorescence doublet (303 and 325 nm) is present in the full SHERLOC spectrum of many sulfate phase detections (Figure 7a). The sum of the fluorescence peak heights for the 303 and 325 nm bands and the sulfate  $\nu_1$  peak height are positively correlated with each other in both Quartier and Bellegarde, although the slope of the relationship is not the same for each target (Figure 7b). The combined PIXL, SHERLOC hydration, and SHERLOC



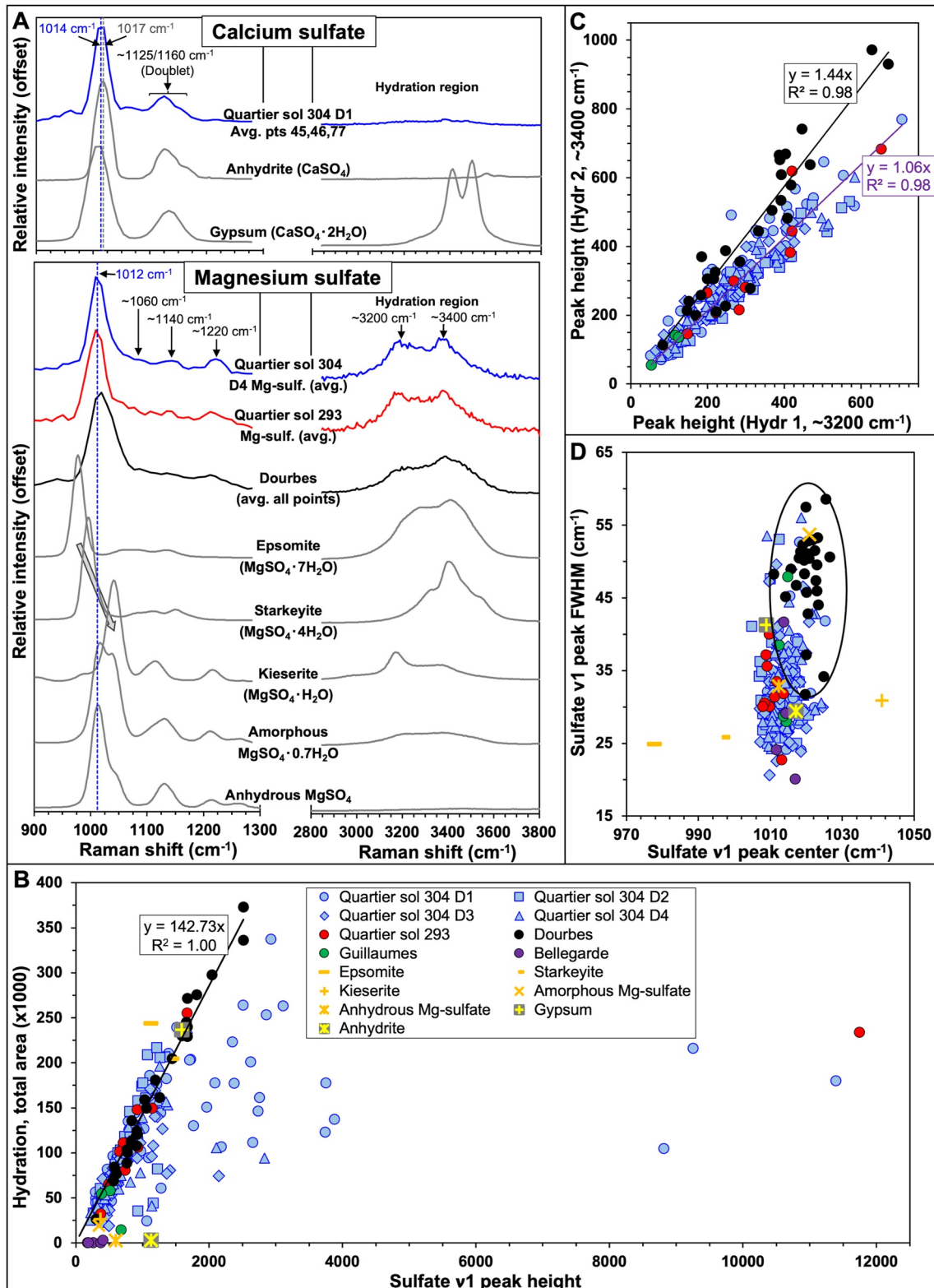


Figure 8.

fluorescence maps of Quartier (Figures 2, 3, and 5) show that fluorescence is typically found in more Ca-rich and less hydrated areas (where HQ is less than 90). The most intense fluorescence detections (>5,000 counts) are associated with very low hydration (HQ < 30) and are found near the border of Ca-rich areas (Figure 3). Fluorescence intensity is also inversely correlated with the HQ value in Quartier (Figure 7c). In Bellegarde, fluorescence is associated with all the SHERLOC sulfate phase detections. None of the spectra of Bellegarde contain hydration and several of these points clearly fall in a Ca-rich area, indicating minimally hydrated Ca-sulfate mineral (possibly anhydrite).

### 3.6. Sulfate $\nu 1$ Peak Height Versus Hydration

Overall, there is a relationship between the sulfate  $\nu 1$  peak heights and the amount of hydration, as indicated by the total area of the bands centered at  $\sim 3,200$  and  $\sim 3,400$   $\text{cm}^{-1}$  (Figure 8). This relationship is strongest in the spectra of sulfate from the Dourbes abrasion, as indicated by the linear regression shown in Figure 8b, with an  $r^2$  value of 1.0. This relationship is virtually identical for most sulfate spectra from Quartier as well and for some points in Guillaumes. This suggests that most of the sulfate minerals in the abrasions have the same degree of hydration except for those that lie to the right of the linear regression in Figure 8b.

## 4. Discussion

### 4.1. Identification of Sulfate Phases

In Quartier, two types of sulfate spectra that correlate well with the PIXL cation distribution can clearly be distinguished. The first group of spectra, obtained from Ca-rich areas, have a sulfate  $\nu 1$  peak at  $1,012$ – $1,020$   $\text{cm}^{-1}$ , a  $\nu 3$  doublet at  $1,125/1,160$   $\text{cm}^{-1}$  and low HQ values (Figures 2 and 3). The sulfate  $\nu 1$  and  $\nu 3$  peak positions match well with those of anhydrite (Figure 8a; Wang et al., 2009). Calculations based on PIXL data indicate sulfate minerals containing  $\sim 1$   $\text{H}_2\text{O}$  in these parts of the sulfate mineral patch. O-H bands are associated with these spectra; however, the positions and shapes of the O-H bands at  $\sim 3,200$  and  $\sim 3,400$   $\text{cm}^{-1}$  observed here are not a good match for either gypsum or bassanite, which have O-H peaks between  $3,400$  and  $3,600$   $\text{cm}^{-1}$  (Figure 8a; Wang et al., 2009). The most likely explanation for the presence of the O-H bands in these spectra is that there are small but variable amounts of hydrated Mg-sulfate phases mixed with the anhydrite, which would also explain the varying HQ values and  $\nu 1$  peak positions.

The second group of spectra, obtained from Mg-rich areas, are characterized by a sulfate  $\nu 1$  peak at  $1,009$ – $1,015$   $\text{cm}^{-1}$ , a slope of overlapping peaks between  $1,040$  and  $1,200$   $\text{cm}^{-1}$ , and a clear peak at  $1,220$   $\text{cm}^{-1}$  (Figure 8a). In some spectra, peaks at  $1,080$  and  $1,140$ – $1,150$   $\text{cm}^{-1}$  can be distinguished in the slope. The fitted  $\nu 1$  peak centers are most consistent with those of a hydrated sulfate phase with three to five waters ( $\text{MgSO}_4 \cdot [3\text{--}5] \text{H}_2\text{O}$ ) such as  $\text{MgSO}_4 \cdot 3\text{H}_2\text{O}$  ( $1,023$   $\text{cm}^{-1}$ ), starkeyite ( $998$   $\text{cm}^{-1}$ ), and pentahydrate ( $1,005$   $\text{cm}^{-1}$ ) (Figure 8a; J. V. Clark et al., 2023; Wang, Freeman, et al., 2006). It should be noted that the exact peak positions for these sulfate phases can be affected by temperatures lower than  $25^\circ\text{C}$  (the temperature at the time of measurement was between  $-50$  and  $-70^\circ\text{C}$ ), causing a shift to higher wavenumbers (Wang et al., 2011). Also, the  $\nu 1$  peak of starkeyite is at a lower wavenumber than expected based on the linear trend of waters versus wavenumber (Figure 8a), likely due to its unique, very compact crystal structure, and thus a Mg-sulfate mineral with four stoichiometric waters would be expected to have a peak center at  $1,011$   $\text{cm}^{-1}$  similar to the value we observe here (Wang, Freeman, et al., 2006). Sulfate minerals with three to five waters also have several weak  $\nu 3$  peaks with the most intense peak

**Figure 8.** Comparison of Scanning Habitable Environments with Raman and Luminescence for Organics and Chemistry (SHERLOC) sulfate spectra and fitted peak parameters with those of sulfate mineral reference samples. (a) The upper panels show a single spectrum (point 77) from the Quartier sol 304 Detail 1 scan in blue, and anhydrite and gypsum samples in gray measured with the MOBIUS instrument (Text S3 in Supporting Information S1) and SHERLOC Brassboard instrument at JPL (Razzell Hollis et al., 2021), respectively. Vertical dashed lines indicate the positions of the  $\nu 1$  peak centers for point 77 and the anhydrite reference sample as determined by peak fitting. The lower panels show average spectra from Mg-sulfate rich areas of the Quartier abrasion (average of all sulfate points in Quartier sol 304 D4, blue spectrum, and selected points from sol 293, red spectrum), the Dourbes abrasion (black spectrum), and five different synthetic Mg-sulfate mineral reference samples analyzed by the ACRONM instrument at JSC (gray spectra; Text S3 in Supporting Information S1; J. V. Clark et al., 2023). Spectra have been normalized to the sulfate  $\nu 1$  peak intensity and offset vertically for clarity. The arrow in the lower left panel shows a general trend of increasing Mg-sulfate  $\nu 1$  peak position with decreasing numbers of structural water molecules. Compare with data from Table 3 and Table S2. (b) Fitted sulfate  $\nu 1$  peak height relative to the total area of the two fitted hydration peaks (The legend in panel (b) applies to panels (c) and (d) as well.) The trendline is fitted to the Dourbes data (black circles). (c) Relationship between the two fitted hydration peak heights (Hydr 1 at  $\sim 3,200$   $\text{cm}^{-1}$  and Hydr 2 at  $\sim 3,400$   $\text{cm}^{-1}$ ). The black trendline is fitted to the Dourbes data points (black circles) and the purple trendline is fitted to all of the Quartier data points (blue and red symbols). (d) Relationship between the fitted sulfate  $\nu 1$  peak center and full width at half maximum.

around 1,140–1,160  $\text{cm}^{-1}$  that could contribute to the slope observed in the spectra (Figure 8a) (Wang, Freeman, et al., 2006). The sharp O-H band at 3,400  $\text{cm}^{-1}$  (e.g., Figure 8a) is also consistent with that of starkeyite. The HQ value (Figure 8c) indicates that the hydration state of Quartier Mg-sulfate minerals falls somewhere between three and five waters ( $\text{MgSO}_4 \cdot [3-5]\text{H}_2\text{O}$ ).

The peak centered at 1,220  $\text{cm}^{-1}$  is not a feature of the spectra of Mg-sulfate phases with three and five waters ( $\text{MgSO}_4 \cdot [3-5]\text{H}_2\text{O}$ ), and in Mg-sulfate minerals is observed only in monohydrated and anhydrous phases (Figure 8a; Culka et al., 2014; Wang, Freeman, et al., 2006). Kieserite has been observed by SuperCam VISIR in both Séítah and Máaz (Mandon et al., 2023) and would explain the sharp O-H peak at 3,200  $\text{cm}^{-1}$  (Figure 8a). However, kieserite is expected to have a  $\nu 1$  peak at 1,040  $\text{cm}^{-1}$  and a  $\nu 3$  peak at 1,115  $\text{cm}^{-1}$  which is not observed in the SHERLOC spectra (Figure 8a). It is possible that a peak at 1,040  $\text{cm}^{-1}$  is not resolved from the  $\nu 1$  peak or that the monohydrated Mg-sulfate phase is amorphous (Figure 8a). However, the spectra of amorphous monohydrated Mg-sulfate minerals are expected to have a double or broad  $\nu 1$  peak, a strong  $\nu 3$  peak at 1,115  $\text{cm}^{-1}$ , and less sharp O-H bands (Figure 8b; Wang, Freeman, et al., 2006; Wang, Haskin, et al., 2006; Wang et al., 2009). None of these features are observed and indicate that any monohydrated Mg-sulfate minerals present in Quartier are not amorphous; this makes kieserite more likely. Taken together, whereas the presence of the 1,220  $\text{cm}^{-1}$  peak cannot be fully explained, the combined data suggest that a complex mixture of more hydrated (three to five waters) and less hydrated (one water) Mg-sulfate minerals are present. This would also be consistent with the approximately three waters calculated from the PIXL data.

The spectra from the Dourbes target match quite well with that of  $\text{MgSO}_4 \cdot 3\text{H}_2\text{O}$  namely the sulfate  $\nu 1$  peak position (1,015–1,025  $\text{cm}^{-1}$  vs. 1,024  $\text{cm}^{-1}$ , respectively) and the presence of  $\nu 3$  peaks at 1,141 and 1,181  $\text{cm}^{-1}$  (Wang, Freeman, et al., 2006; Wang et al., 2009). The hydration shape is also similar to that of a hydrated Mg-sulfate phase with three waters (Wang, Freeman, et al., 2006) and the HQ values also fall in between the values of starkeyite and kieserite, consistent with the three waters (Figure 8). The  $\nu 1$  peak is broader in Dourbes than for other targets (Figure 8d). This observation could be explained by the presence of amorphous Mg-sulfate phases, which have broader or multiple peaks (Figure 8; Wang, Freeman, et al., 2006). Similar to those of Quartier, the spectra of Dourbes contain a peak at 1,220  $\text{cm}^{-1}$  that indicates the presence of monohydrated or anhydrous Mg-sulfate phases. Although the  $\nu 1$  peak is a good match to the amorphous monohydrated Mg-sulfate phase in Figure 8, the  $\nu 3$  peak at 1,115  $\text{cm}^{-1}$  is missing and the relatively intense peak at 3,400  $\text{cm}^{-1}$  is inconsistent with this phase. The HQ indicates the hydration state is closer to four waters than one and is similar to that of Quartier (Table 3). PIXL-based hydration calculations from this area are highly variable, indicating between one and six waters, most likely due to the presence of varying amounts of carbonate phases intermixed with the sulfate phase, which makes it difficult to accurately estimate the hydration state using that method. PIXL analyses also indicate the presence of both Mg-sulfate and Ca-sulfate phases in Dourbes (Tice et al., 2022).

In the Bellegarde target, several of the SHERLOC sulfate mineral detections are clearly located in the area indicated by PIXL as a Ca-sulfate phase. The sulfate  $\nu 1$  peak in the spectrum from this area is at 1,008–1,017  $\text{cm}^{-1}$  and the lack of detectable hydration is consistent with a less hydrated Ca-sulfate mineral such as anhydrite. Unfortunately, due to low signal counts, the  $\nu 3$  peaks are very weak if present and are not necessarily diagnostic. It is possible that hydration was not detected in Bellegarde due to low Raman signals (180–408 counts). This hypothesis can be tested using the linear fit of hydration intensity relative to sulfate  $\nu 1$  peak intensity for Dourbes ( $y$  [hydration intensity] = 142.73 $x$  [sulfate  $\nu 1$  intensity]; Figure 8b). If the Bellegarde sulfate minerals were as hydrated as the Mg-sulfate minerals from Dourbes, the average fitted  $\nu 1$  peak height for Bellegarde (261 counts) would be expected to have a total hydration peak area of  $\sim 37,000$ . This value is more than two times greater than that of the hydration features in Guillaumes ( $\sim 14,000$ ) that are clearly observable in the spectra (Point 66, Figure 6; Table S5 in Supporting Information S1). From this it can be assumed that any hydration peaks in Bellegarde hidden in the noise would have an area of less than 10,000 counts, which would result in HQ values less than 38. This value is similar to the areas in which some of the strongest anhydrite detections occur in Quartier (Table S3 in Supporting Information S1). In addition to the Ca-sulfate phase observed by SHERLOC and PIXL, the PIXL data also indicated the presence of Mg-sulfate phases (Table 2, Figure 5).

In Guillaumes, the SHERLOC sulfate  $\nu 1$  peak centers fall between 1,013 and 1,015  $\text{cm}^{-1}$ , which is consistent with hydrated Mg-sulfate minerals or anhydrite. Due to mixing with perchlorate phase (Corpolongo et al., 2023), which have  $\nu 3$  peaks in the same region as those of sulfate minerals, it is difficult to identify which, if any, comes from sulfate minerals relative to the perchlorate phase. The one sulfate spectrum that does not contain peaks from



a perchlorate phase contains no clear  $\nu_3$  peaks and has a hydration peak which falls on the same hydration line as Quartier and Dourbes (Figure 8b). The shape of the O-H bands in Guillaumes with two distinct O-H peaks at  $\sim 3,200$  and  $\sim 3,400$   $\text{cm}^{-1}$  is similar to what is observed in Quartier. Two of the points of Guillaumes fall on the Dourbes hydration line while one falls off and one does not have a clear hydration signal (Figure 8b). In PIXL data sets, both Mg- and Ca-sulfate minerals were detected, and calculations indicate a hydration state of less than one water in the Ca-sulfate mineral (due to low amounts of Mg-sulfate minerals it was not possible to calculate hydration for those). Based on the comparison with the other targets, it seems likely that Guillaumes is a mixture of anhydrite (or less likely bassanite as hydration bands typical for bassanite were not detected) and a hydrated Mg-sulfate phase with three to five waters (Wang et al., 2009).

Major contributions from Na-sulfate and Fe-sulfate minerals to the sulfate spectra of all four abrasions can be ruled out. Based on PIXL analyses, there is only  $\sim 2\%$  Na present in the targets and even anhydrous Na-sulfate spectra have a  $\nu_1$  peak position at lower wavenumbers ( $< 1,000$   $\text{cm}^{-1}$ ) than was measured for these targets (Hamilton & Menzies, 2010). There is  $< 2\%$  Fe in the Mg-rich areas of Quartier, and Fe-sulfate minerals typically produce low intensity spectra with the DUV laser of SHERLOC (Razzell Hollis et al., 2021). The SHERLOC spectra from Mg-rich regions with varying amounts of Fe concentrations in Quartier and Dourbes look similar, both in peak positions and shapes (Figures 2–4), which suggests that the sulfate phases in each have similar cation compositions, and that the Fe is mostly associated with other mineral phases. Analysis of the PIXL elemental data suggest that most Fe in these targets is associated with carbonate and silicate phases (Tice et al., 2022). It is possible that the Mg-sulfate phases contain minor components of Fe and Na in solid solution, which would shift the  $\nu_1$  peak to a lower wavenumber than the corresponding pure Mg-sulfate phase with the same amount of bound water (Hamilton & Menzies, 2010; Talla & Wildner, 2019). Other Fe-sulfate phases, such as jarosite, can be excluded based on low concentrations of Na (2%) and K ( $< 1\%$ ) in these areas, and these phases typically contain double  $\nu_1$  peaks (Chio et al., 2005).

#### 4.2. Hydration Stability and Implications for the Water Cycle on Mars

The sulfate phases detected by SHERLOC and PIXL in crater floor rocks are most consistent with hydrated crystalline and amorphous Mg-sulfate minerals with three to five waters ( $\text{MgSO}_4 \cdot [3-5]\text{H}_2\text{O}$ ) mixed with possible monohydrated crystalline and amorphous Mg-sulfate minerals ( $\text{MgSO}_4 \cdot \text{H}_2\text{O}$ ) and anhydrous Ca-sulfate minerals. Laboratory experiments on Earth have shown that Mg-sulfate can form complex mixtures with varying amounts of hydration, including, for example, those that contain 2.4 waters and a mix of crystalline and amorphous phases (Chipera & Vaniman, 2007; Wang, Freeman, et al., 2006). The Mg-sulfate phases detected here are in the hydration range of starkeyite, which has been suggested to be the most stable Mg-sulfate phase under Martian surface conditions near the equator (Chipera & Vaniman, 2007; Wang et al., 2009; Wang et al., 2016). In addition, this is consistent with the recent identification of starkeyite at Gale crater (Chipera et al., 2023). MEDA measurements of local temperature, humidity and pressures in Jezero crater at the time of collection of these data also confirm that starkeyite would most likely have been stable (Hausrath et al., 2023).

Amorphous Mg-sulfate phases such as those identified in the Dourbes abrasion are suggested to form from the dehydration of  $\text{MgSO}_4 \cdot n\text{H}_2\text{O}$  when exposed to a hyperarid environment like that on the surface of Mars or via evaporation during deposition (Wang et al., 2016). This might explain why the widths of the Mg-sulfate  $\nu_1$  peaks of the Dourbes target are broader and at higher wavenumbers than those of the Quartier target (Figure 8d) as well as the less distinct peak at  $\sim 3,200$   $\text{cm}^{-1}$  (Figure 8a), indicating the possible presence of an amorphous Mg-sulfate phase with three water molecules (Wang, Freeman, et al., 2006; Wang et al., 2009). These observations are consistent with experimental results that demonstrate amorphous Mg-sulfate phases can hold a maximum of three waters (Wang et al., 2009) and with results from the CheMin instrument on the Curiosity rover in Gale crater that indicate a large portion of the Mg-sulfate phases are XRD amorphous (Smith et al., 2022). We note that the sulfate phases in Gale crater and elsewhere on Mars, as detected by orbiters and Curiosity, are in sedimentary rocks as opposed to being a component of altered igneous rock like the sulfate from Jezero crater discussed here. Despite this difference in origin, they show similar hydration states, suggesting that the hydration state is controlled by current surface environmental conditions.

MEDA measurements suggest that early morning ground surface relative humidity and temperature can, if kinetics permit, allow for the hydration of Mg-sulfate minerals by seven water molecules (epsomite). Given that the hydration–dehydration cycle is not instantaneous, and the ground–atmosphere interaction may be out of equilibrium, this higher hydration state may persist through more hours of the day (see Figure 6 of Hausrath et al., 2023). The SHERLOC and PIXL measurements were performed in the evening and at night when relative humidity is

less than 2%, under which conditions it is predicted that sulfate minerals more hydrated than starkeyite is not stable (Hausrath et al., 2023).

It is possible that the duration between abrasion and the SHERLOC scans (a minimum of one sol) was sufficient for the partial dehydration of sulfate minerals from higher hydration states such as epsomite, meridianiite, and gypsum, which would mean these results underestimate how much water was bound in the sulfate phases before abrasion and exposure. Experiments show that epsomite is stable in pure Mg-sulfate mineral mixtures at lower temperatures (at RH = 7% and 5°C) for at least 37 hr and is only converted to hexahydrate after 300 hr (the longest time between abrasion—Dourbes—and the performance of a SHERLOC scan) (Chipera & Vaniman, 2007; Wang et al., 2009). The same experiments show that adding anhydrite or chloride phases to the mixture slows this process and that gypsum and bassanite were unaffected by even higher temperatures (50°C; Wang et al., 2009, 2016), although recent experiments on the Curiosity rover indicate that gypsum dehydrated to bassanite inside the rover over 20 days (at up to 30°C) (Vaniman et al., 2018). The maximum temperature experienced by the abrasions was 10°C at RH <2%; however, this was experienced by the sample for only a few hours during the sol (Polkko et al., 2023). Also, the relatively high thermal inertia (~370–600) of the rocks would have slowed the heat transfer to the rock, maintaining a temperature lower than the maximum measured local air temperature (Martinez et al., 2023; Vaniman et al., 2018). Consequently, the hydration state of the sulfate phases identified here likely did not change during the first sol after abrasion. In addition, this is consistent with the fact that no major spectral changes ( $\nu 1$  peak position and width, position or shape of O-H bands and HQ values) were observed in the Quartier data sets between the scans acquired even 11 sols apart, indicating that the sulfate phases were relatively stable during this time (Table 2, Figure S1 in Supporting Information S1).

Notably, Dourbes was scanned 16 sols after the abrasion and therefore had a longer time than the other targets to re-equilibrate with the Martian atmosphere. Experiments have also shown that the presence of mineral phases with other cations, such as iron-containing minerals in Dourbes, would increase the dehydration rates of hydrated Mg-sulfate minerals (Wang et al., 2016). This could explain the apparent lower hydration of Dourbes sulfate minerals than those of Quartier based on shifted  $\nu 1$  peak position, although the lower hydration is not observed in the calculated HQ values. It has been proposed that higher purity Mg-sulfate fluids will precipitate epsomite, which will dehydrate to starkeyite, whereas lower purity fluids will dehydrate to monohydrated Mg-sulfate phases (Wang et al., 2009, 2016). However, the Mg-sulfate phases analyzed here appear to have similar hydration in more and less pure Mg-bearing areas in both Quartier and Dourbes.

The results from both Séítah and Máaz show that hydrated Mg-sulfate and anhydrous Ca-sulfate species occur in close (sub-millimeter) proximity. This association has been previously observed (though at different spatial scales) in Gale crater where gypsum, bassanite, and anhydrite appear together, and in orbital data where monohydrated and polyhydrated sulfate phases appear in alternating meter-scale layers (Ehlmann & Edwards, 2014; Gendrin et al., 2005; Vaniman et al., 2018). Contrary to previous Ca-sulfate mineral detections on Mars, where Ca-sulfate minerals of different hydration states has been identified (Nachon et al., 2014; Vaniman et al., 2018), only anhydrite was detected in the floor units of Jezero crater. One possibility is that the Ca-sulfate phase was originally deposited as gypsum that then dehydrated to anhydrite (Vaniman & Chipera, 2006; Vaniman et al., 2018). Dehydration of gypsum to anhydrite is slow even at higher temperatures (85°C), especially in rocks with higher thermal inertia and low albedo in the subsurface such as the abrasions of Máaz and Séítah (Marion et al., 2016; Martinez et al., 2023; Rapin et al., 2019; Robertson & Bish, 2013). Also, the temperature in the subsurface is lower than at the surface (Rapin et al., 2019). On Earth, primary anhydrite typically forms at elevated temperatures (>50°C) such as in hydrothermal systems; however, it has been shown that anhydrite may precipitate from solution at lower  $T$  (0°C) and low water activity (Marion et al., 2016; Miller, 2017), which indicates that this anhydrite precipitated from a saline fluid.

The identification of  $\text{MgSO}_4 \cdot [3-5] \text{H}_2\text{O}$  puts a lower constraint on how much water is contained in polyhydrated sulfate minerals in the near subsurface at the equator and can help explain the amount of hydrogen detected by OMEGA (Wang, Freeman, et al., 2006; Wang et al., 2016). It has been estimated that 1 kg of starkeyite can hold 0.6 kg of water (Chou & Seal, 2007). The identification of hydrated phases is important for the general understanding of volatile sequestration on Mars and the evolution of surface habitability (Mustard, 2019; Scheller et al., 2021).

### 4.3. Formation of Sulfate Minerals and the Relationship to Sulfate Minerals in the Fan and Elsewhere on Mars

It is not clear whether the Mg-sulfate or Ca-sulfate minerals in Mááz and Séítah formed first. If they precipitated from the same solution, the Ca-sulfate minerals should have precipitated first and the Mg-sulfate minerals later due to the lower solubility of Ca-sulfate phases (Lide, 2004; Tosca & McLennan, 2006). If they formed in two separate events, the Mg-sulfate minerals could have formed first with some later replaced with Ca-sulfate minerals. The dissolution of Mg-sulfate minerals by later Ca-containing saline fluid would rapidly come to a halt as Ca-sulfate minerals are precipitated, resulting in a mixture of Mg-sulfate and Ca-sulfate phases (Rapin et al., 2019). The Quartier abrasion features areas with only hydrated Mg-sulfate phases, whereas all Ca-sulfate phases occur in mixed anhydrous Ca-sulfate/hydrated Mg-sulfate areas. In contrast, the Bellegarde and Dourbes abrasions feature areas with only anhydrous Ca-sulfate minerals (Figure 5; Tice et al., 2022). Notably, the Séítah formation seems to have a higher proportion of Mg-sulfate minerals relative to Ca-sulfate minerals than the Mááz formation.

Several different scenarios for the formation of the sulfate phases seem possible based on the observed sulfate mineral distributions and hydration. One is that hydrated Ca- and Mg-sulfate phases, such as gypsum and epsomite/meridianiite (depending on the temperature during deposition), precipitated from the same solution with Ca-sulfate minerals precipitating first (McLennan, 2012; Peterson & Wang, 2006; Tosca & McLennan, 2006). These would then have dehydrated to  $\text{MgSO}_4$  with three to five waters and anhydrite over time. Another possibility is that the sulfate minerals precipitated from a hydrothermal or highly saline fluid, depositing anhydrite followed by hydrated Mg-sulfate phases. The formation from hydrothermal fluids could explain the possible detection of kieserite in Quartier. Yet another possibility is that hydrated Mg-sulfate minerals, such as epsomite or meridianiite, were deposited first, with later precipitation of hydrated/anhydrous Ca-sulfate minerals from a separate fluid. Depending on the original hydration state of the sulfate phases, they might then have over time dehydrated to Mg-sulfate with three to five waters and anhydrite.

The textures of the observed sulfate mineral-bearing regions can further facilitate the interpretation of the environment of sulfate mineral deposition. In all examples described here, sulfate phases occur as irregular patches across the abraded surface, where they occur interstitially between discrete regions of host rock and within primary void space; such distribution favors an interpretation that the sulfate-bearing fluid was a post-emplacement fluid. In the Bellegarde abrasion, a brown-weathering iron-rich phase that occurs as a first generation, cement lining primary voids shows the clearest evidence for the timing of this fluid interaction (Figure 5a; see also Figure 11 of Wogslund et al., 2023). Sulfate phases in the Bellegarde target nearly exclusively occur as the final stage of mineral precipitation within these voids, consistent with late-stage fluid flow.

Evidence for the potential environment of this post-depositional fluid (i.e., surficial fluid with low temperature precipitation vs. burial fluid at low- or high-temperatures) is less well constrained. Sulfate mineral-bearing phases appear either as groups of discrete, large (often mm-scale) crystals (Quartier and Bellegarde, see Figures 2a, 3a, and 5a) or patches with no resolvable individual crystals (all abrasions). Large crystals of sulfate minerals are often associated with higher-temperature, hydrothermal, or burial conditions where nucleation rates are typically low relative to crystal growth rates. However, similar large crystals (e.g., poikilitic gypsum minerals in terrestrial sedimentary rocks) are commonly associated with crystal growth at low temperatures in both fluid-saturated environments of the shallow subsurface and fluid-poor surficial environments, where elevated saturation states drive high rates of crystal growth (cf. Kah et al., 2018; Mees et al., 2012; Watson, 1985).

In both Séítah targets, the detected sulfate phases are closely associated with other alteration minerals such as Mg/Fe-carbonate, low (Fe, Mg) silicate, and perchlorate/chlorate/phosphate phases with the carbonate minerals surrounding the sulfate minerals in Quartier and Dourbes (Corpolongo et al., 2023; Tice et al., 2022). In the Guillaumes and Bellegarde abrasions, the sulfate phases are associated with iron and perchlorate/chlorate/phosphate phases, identified as Na-perchlorate phases in Guillaumes (Corpolongo et al., 2023; Scheller et al., 2022; Wogslund et al., 2023). Comparing the results in this paper with earlier works shows that there is no systematic association between either Mg- or Ca-sulfate minerals and any of the other alteration minerals in either Séítah or Mááz (Corpolongo et al., 2023; Tice et al., 2022).

The spatial and paragenetic relationship between the different minerals in Séítah noted above, namely sulfate phases surrounded by carbonate phases, suggests that the carbonate phases were formed first, probably by



carbonation or serpentinization of the host rock, which also formed the various low (Fe, Mg) silicate minerals present (Tice et al., 2022). Sulfate minerals then might have formed later from a slightly acidic sulfate-rich fluid (Mandon et al., 2023; Tice et al., 2022), which dissolved the cores of some of the carbonate mineral deposits, into which the sulfate minerals precipitated. However, it has also been interpreted as the result of sulfate-rich fluid filling the void left after the carbonate alteration (Tice et al., 2022). In Quartier, the Ca-sulfate phases are found in close proximity with Ca-pyroxene, indicating a possible source for the Ca (Figures 2 and 3 and Figure S1 in Supporting Information S1). However, this is not observed for other targets, and it has therefore been suggested that the Ca and Mg in the sulfate minerals is allochthonous (Tice et al., 2022). In addition, Mg-sulfate phases in Séítah and Máaz have a higher Mg/Fe ratio (90:10) than the surrounding igneous minerals such as the olivines (55:45), indicating that these sulfate minerals did not form in situ but were deposited from a sulfate-rich fluid that transported the cations in from elsewhere (Figure S2 in Supporting Information S1; Liu et al., 2022; Tice et al., 2022). This is different from, for example, the Burns formation in Meridiani Planum on Mars, where sulfate minerals have a ratio of cations that is similar to their host rock and are therefore suggested to be formed in situ from, for example, acid-sulfate alteration (McCullom, 2018). Interestingly, some parts of the Burns formation seem to have experienced loss of the more soluble Mg-sulfate minerals, which were suggested to have deposited in the underlying unit (McCullom & Hynke, 2021); similar mobilization from mixed sulfate phases elsewhere may have supplied Mg-sulfate-rich fluids to Jezero crater floor rocks. The absence of Fe-sulfate phases in the crater floor rocks suggests moderate pH due to the low mobility of Fe under less acidic conditions (Rapin et al., 2019; Tosca & McLennan, 2006). Additionally, alteration of olivine with little-to-no alteration of feldspar and pyroxene in the Seitah formation (Liu et al., 2022; Tice et al., 2022) is consistent with fluid interactions at broadly circumneutral pH (Hausrath & Brantley, 2010; Hausrath et al., 2008). The lack of alteration of pyroxene and feldspar, together with the association of sulfate minerals with carbonate minerals and low (Fe, Mg) silicate minerals inferred to have formed at low temperatures, also seem consistent with the sulfate minerals observed in the crater floor having been deposited from a low temperature sulfate-rich fluid (Tice et al., 2022). The presence of Mg-sulfate minerals typically means that the fluid was saline (Tosca & McLennan, 2006; Tosca et al., 2008). Perchlorate mineral formation likely happened last due to the instability of these phases in water (Scheller et al., 2022; Tice et al., 2022).

Assuming that all of the white patches in abrasions are composed of sulfate minerals, Quartier contains more these phases than the other targets of Séítah, Dourbes and Garde (no sulfate minerals were detected in the latter; Figure 1; Corpolongo et al., 2023). Quartier is stratigraphically higher than Dourbes and Garde and therefore was previously closer to the stratigraphically overlying Máaz fm., which experienced sulfate alteration similar to Séítah (Horgan et al., 2023). In Máaz, sulfate phases were mainly detected in Guillaumes and Bellegarde. Multispectral studies by PIXL and ZCAM indicate that the higher members of the two formations are more altered in terms of oxidation than the lower units (Horgan et al., 2023; Pedersen et al., 2022). In Séítah, the most oxidized targets also contain the most visible signs of sulfate mineral deposition (Figure 1). However, in Máaz, sulfate minerals were only weakly detected in the Alfalfa abrasion ( $\text{SO}_3 < 1 \text{ wt}\%$ ) (Ch'af member), which appears to be the most oxidized abrasion target of the Máaz formation as observed by PIXL and ZCAM multispectral (although the lack of sulfate mineral detections could be due to sampling bias). This suggests two things: (a) it was not the same event that deposited the different sulfate phases and oxidized the rocks; and (b) the sulfate mineral deposition in Séítah and Máaz are unrelated. It is likely the precipitation of sulfate minerals in all Séítah rocks occurred during the same event affecting the uppermost members more than underlying ones, indicating that the sulfate-rich fluid came from above rather than below. In Máaz, the sulfate mineral deposition seems to have been more sporadic considering that it is not detected as extensively in the whole formation. These observations seem to suggest numerous events of sulfate mineral deposition, likely from a low temperature, moderate pH saline fluid during the time that water was still present at Jezero crater. The exact origin of the sulfate-rich fluids that deposited the sulfate minerals in the crater floor is unknown. They could have originated from the remobilization of sulfate minerals from sedimentary sulfate deposits that seem widespread in Jezero crater, including in the delta fan front, or from other unknown sources, including magmatic, volcanic, or hydrothermal sulfate deposits (Hurowitz et al., 2023).

The sulfate phases detected in the crater floor rocks are mainly hydrated Mg-sulfate and anhydrous Ca-sulfate minerals. The main sulfate phases in the delta fan are hydrated Mg/Fe-sulfate with anhydrous Ca-sulfate minerals formed during later diagenetic alteration (Hurowitz et al., 2023). This observation indicates that the sulfate-rich fluids that deposited the sulfate phases in the crater floor rocks had different chemistry than the fluids that deposited sulfate minerals at the delta, making them distinct alteration events. Evidence for at least two distinct sulfate

mineral formation events supports the idea that multiple events of sulfate-rich fluids of different compositions operated in Jezero crater during a time period bordering the Noachian/Hesperian.

#### 4.4. Sulfate Phases and Doublet Fluorescence

Fluorescence signals, which are detected in Bellegarde and Quartier, show a positive correlation with sulfate mineral Raman peak intensity for each target (Figure 7). This strengthens the case that this particular fluorescence signal is associated with sulfate minerals, as previously argued (Sharma et al., 2023). The data from Quartier and Bellegarde (Figures 2, 3, 5, and 8) show that the doublet fluorescence is preferentially located with the less hydrated Ca-sulfate minerals for both targets. Bellegarde showed much higher fluorescence intensity relative to sulfate  $\nu_1$  intensity than Quartier (Figure 7b), possibly because the sulfate phases in this target are mainly anhydrite compared with Quartier, which has a mix of anhydrite and hydrated Mg-sulfate minerals. Dourbes, on the other hand, which only contains hydrated Mg-sulfate phases, did not show any doublet fluorescence, strengthening the case that the anhydrite is the carrier of fluorescence. The only target that did not follow this trend was Guillaumes, which seemed to contain anhydrite but had no associated doublet fluorescence.

The association between the doublet fluorescence signal and anhydrite provides insight into the origin of the fluorescence signal, specifically about whether it is from organic or inorganic sources such as  $Ce^{3+}$  or a mixed organic/inorganic source (Sharma et al., 2023).  $Ce^{3+}$  has been shown to produce a doublet fluorescence in anhydrite (Baumer et al., 1997; Gaft & Raichlin, 2020), which seems to be the bearer of the doublet in the crater floor rocks. The shape and exact position (304 and 327 nm, 318 and 338 nm) of the doublet in previous work (Baumer et al., 1997; Gaft & Raichlin, 2020) is slightly different from the doublet observed here (303 and 325 nm). Previously, an association of sulfur and organic compounds was observed at Gale crater where Curiosity detected abundant S-bearing organics and heteroatoms released during pyrolysis from a macromolecular organic structure (Eigenbrode et al., 2018; Millan et al., 2022). Currently, the SHERLOC team is investigating both the inorganic and organic hypotheses for the fluorescence observed in Jezero crater.

#### 4.5. Considerations for Sample Return Science

The Perseverance rover has collected samples adjacent to the abraded patches studied here (Simon et al., 2023), which were hermetically sealed and are now stored in two caches, one on the surface of Mars, and the other onboard the rover. The processes of coring and sealing, and subsequent storage on Mars have subjected and will continue to subject these samples to fluctuations in temperature and humidity. The rover systems are designed to heat samples as little as possible during coring, sealing, and storage:  $\leq 60^\circ C$  during coring (mission requirement; Farley et al., 2020), transient heating to  $\leq 40^\circ C$  during sealing of sample tubes (though samples likely experienced much less; Farley & Stack, 2022), up to  $\sim 28^\circ C$  during storage of samples in the surface cache (Farley et al., 2020), and  $\sim -20^\circ C$  for samples stored in the rover (PDS). Considering the sensitivity of sulfate minerals to dehydration and rehydration and the possibility of other phases in the samples that could trap evolved water, it is possible that sulfate minerals will not preserve their original hydration state and information about the past and present hydrological cycle of Mars could be lost (Vaniman et al., 2004, 2018). Therefore, it is of the utmost importance to understand the in situ data collected from the sulfate minerals by the Perseverance rover on Mars and compare these data to laboratory measurements following sample return. Further laboratory experiments on Earth would be required to study the effects of sulfate mineral mixtures and temperature on Raman spectral peak positions and intensities to understand the exact composition of the sulfate phases. This is also needed to better understand the potential for hydration and rehydration at different timescales and the formation of the sulfate minerals detected.

Despite the possibility of alteration during storage and transport, having samples of martian materials on Earth of known geologic and paleoenvironmental context will allow for the use of laboratory instruments to probe chemical, isotopic, and sub-micron scale morphological signatures not possible with current rover technology. Such studies will allow us to determine or constrain the modes of formation and alteration of the crater floor units, both of which are critical for interpreting geochronological data from the igneous floor units. Detailed chemical and isotopic analyses of sulfate minerals in the returned samples can also help determine and/or constrain the properties of the waters from which they precipitated at multiple scales. At a local scale, chemical and isotopic analyses can reveal water temperature, pH, and salinity, which can help constrain the original source of the fluids

from which the sulfate minerals precipitated (e.g., lacustrine, hydrothermal; e.g., Franz et al., 2017; Ono, 2017; Seal et al., 2000; Scheller et al., 2022; Simon et al., 2023). At a broader scale, understanding the chemistry of the sulfate minerals, their geological context, and the timing of their deposition could help constrain Mars' climatic history, hydrological cycle, and sulfur cycle (e.g., Bibring et al., 2006; Milliken et al., 2010; Vaniman et al., 2004).

Additionally, sulfate minerals in returned samples of the crater floor units could be studied for their biosignature potential. Although no definitive biosignatures are reported here from sulfate minerals or other phases within the crater floor units, hydrated sulfate minerals have been reported to be habitable niches for terrestrial endolithic life and also a means of preserving biosignatures. Microorganisms, including cyanobacteria, can use gypsum ( $\text{CaSO}_4 \cdot 2\text{H}_2\text{O}$ ) as a substrate, demonstrating that microbes could extract water from hydrated salts in the rock, inducing a phase transformation from gypsum to anhydrite ( $\text{CaSO}_4$ ) (Huang et al., 2020; Wierzchos et al., 2011). In addition, in terrestrial analogs, many metabolic pathways have been identified in association with sulfate mineral deposits, including microbial sulfate reduction and photosynthetic and non-photosynthetic sulfur and sulfide oxidation. Thus, during and after the final drying of Lake Jezero, sulfate minerals may have been among the last habitable localized paleoenvironments at Jezero crater.

Not only do sulfate minerals provide habitable conditions, but they also have a high biosignature preservation potential. They can trap and preserve microorganisms and organic compounds within solid and fluid inclusions (Benison, 2019; Benison & Karmanocky, 2014; Bowden & Parnell, 2007; Dela Pierre et al., 2015; Gill et al., 2023) providing a microenvironment to protect them from oxidation and radiation-induced decay enabling their survival over geologic time scales (Lowenstein et al., 2011; Schreder-Gomes et al., 2022). Terrestrial microfossils have also been discovered in ~260-million-year-old sulfate mineral (gypsum) deposits (Schopf et al., 2012). Importantly, Mg- and Ca-sulfate minerals, the dominant types in the Jezero crater floor units, preserve organic matter better than  $\text{Fe}^{3+}$ -bearing sulfate phases (e.g., jarosite), which exist in other regions of Mars (Farrand et al., 2009; Klingelhöfer et al., 2004) under martian burial temperatures and timescales (Tan & Sephton, 2020).

## 5. Conclusions

The sulfate minerals from the crater floor rocks of Jezero crater are characterized by mixtures of crystalline and amorphous Mg-sulfate minerals with three to five waters mixed with possible amorphous and crystalline monohydrated Mg-sulfate minerals and anhydrous Ca-sulfate minerals. The results also show that these sulfate minerals are stable even after being exposed to Martian atmospheric conditions up to as much as 11 to 16 sols. These results are consistent with what is predicted by experiments on Earth for which hydrated sulfate minerals should be stable at the equator on Mars. More importantly, it puts a lower constraint on how much water the pool of sulfate minerals contains in the shallow subsurface, which is important for understanding the distribution of water on Mars generally and constraining the hydrological cycle. The distribution of sulfate phases in the Jezero crater floor indicates that they were deposited at moderate pH and low temperature during multiple events.

The doublet fluorescence feature previously identified was confirmed to be associated with sulfate minerals and specifically with anhydrite which provides insight to the origin of this signal.

Finally, although the hydration state of the sulfate minerals in collected samples may change during storage on Mars inside the sample tubes, sulfate minerals are key samples for future return to Earth to better understand the past climate, hydrological cycle, and potential for past life on Mars.

## Conflict of Interest

The authors declare no conflicts of interest relevant to this study.

## Data Availability Statement

The data used in this publication include rock target close up images (WATSON, Figures 1–6, 1014 NASA PDS <https://doi.org/10.17189/1522643>, Beegle et al., 2021) X-ray fluorescence data 1015 (PIXL, Figures 2–6; Table 1, Figure S1 in Supporting Information S1 and Table S2, Tables S3 and S4 in Supporting Information S1, NASA PDS 1016 <https://doi.org/10.17189/1522645>, Allwood & Hurowitz, 2021), Raman and



fluorescence data 1017 (SHERLOC, Figures 2–8, Tables 2–3, and Table S1 in Supporting Information S1 and Table S5, NASA 1018 PDS <https://doi.org/10.17189/1522643>, Beegle et al., 2021), and atmospheric data (MEDA, 1019 NASA PDS <https://doi.org/10.17189/1522849>, Rodriguez-Manfredi et al., 2021). 1020 Software packages used in this publication for SHERLOC data include Loupe (version v.5.1.5, 1021 Uckert, 2022, Zenodo <https://doi.org/10.5281/zenodo.7062998>) and peak fitting program Fityk 1022 (version v.1.3.1; Wojdyr, 2010, <https://fityk.nieto.pl/>). 48 1023 PIQUANT (Version v3.2.11, Elam & Heirwegh, 2022, Zenodo: 1024 <https://doi.org/10.5281/zenodo.6959125>), PIXLISE Core (Version v2.0, Nemere et al., 2022a, 1025 Zenodo <https://doi.org/10.5281/zenodo.6959096>) and PIXLISE UI (Version v2.0, Nemere et al., 2022b, 1026 Zenodo <https://doi.org/10.5281/zenodo.6959109>) were used to treat PIXL data.

#### Acknowledgments

We would like to thank the Mars 2020 Perseverance Science and Engineering teams for their work on the mission that has enabled the analysis of the crater floor targets. We also thank two anonymous reviewers who provided substantive feedback on a previous version of this paper. The work described in this paper was partially carried out at the Jet Propulsion Laboratory, California Institute of Technology, under a contract with the National Aeronautics and Space Administration. S.S. acknowledges funding from the Swedish National Space Agency (contracts 2021-00092 and 137/19). A.D.C. and A.C. were supported by the Mars 2020 Returned Sample Science Participating Scientist Program (NASA award number 80NSSC20K0237), and A.C. was additionally supported by a National Science Foundation Graduate Research Fellowship (award number 2035701). AYL was supported by subcontract number 1655697 from JPL (from NASA as part of the Mars 2020 Phase E funding). BLE and YP were supported by NASA Mars 2020 Co-Investigator funds to support BLE on SHERLOC. KCB was supported by the Mars 2020 Returned Sample Science Participating Scientist Program (NASA award number 80NSSC20K0235). ASB was supported by the Mars 2020 Mission. TF was supported by the ASI/INAF agreement 2023-3-HH.0. NCH was supported by the JETS II contract with Johnson Space Center. NASA. KHL was supported by the UK Space Agency Aurora Research Fellowship (ST/V00560X/1). RSJ acknowledges funding from an Advanced Curation project run by the NASA Astromaterials Acquisition and Curation Office, Johnson Space Center. RVM was supported by the ISFM Mission Enabling Work Package at the Johnson Space Center. MM was supported by a contract with NASA/JPL (1685477). MAS was supported by UK Space Agency Grants ST/V002732/1 and ST/V006134/1. SKS acknowledges Mars 2020 SuperCam Co-PI support and contract with NASA/JPL (1654163). SVB was supported by the Mars 2020 Participating Science Program, Grant 80NSSC21K0328. AJW was supported by the NASA Mars 2020 Participating Scientist Program, Grant 80NSSC21K0332. AY was supported by a contract with NASA/JPL (1651660). MPZ was supported by Grant PID2019-104205GB-C21 funded by MCIN/AEI/10.13039/501100011033.

#### References

- Allwood, A. C., & Hurowitz, J. A. (2021). *Mars 2020 PIXL bundle*. NASA Planetary Data System. <https://doi.org/10.17189/1522645>
- Allwood, A. C., Wade, L. A., Foote, M. C., Elam, W. T., Hurowitz, J. A., Battel, S., et al. (2020). PIXL: Planetary instrument for X-ray lithochemistry. *Space Science Reviews*, 216(8), 1–132. <https://doi.org/10.1007/s11214-020-00767-7>
- Andrews-Hanna, J. C., Phillips, R. J., & Zuber, M. T. (2007). Meridiani Planum and the global hydrology of Mars. *Nature*, 446(7132), 163–166. <https://doi.org/10.1038/nature05594>
- Banin, A., Han, F. X., Kan, I., & Cielosky, A. (1997). Acidic volatiles and the Mars soil. *Journal of Geophysical Research*, 102(E6), 13341–13356. <https://doi.org/10.1029/97je01160>
- Baumer, A., Blanc, P., Cesbron, F., & Ohnenstetter, D. (1997). Cathodoluminescence of synthetic (doped with rare-earth elements) and natural anhydrites. *Chemical Geology*, 138(1), 73–80. [https://doi.org/10.1016/s0009-2541\(96\)00175-1](https://doi.org/10.1016/s0009-2541(96)00175-1)
- Beegle, L. W., Bhartia, R., Deen, R. G., Padgett, D., Algermissen, S., Dunn, A. E., et al. (2021). *Mars 2020 SHERLOC bundle*. NASA Planetary Data System. <https://doi.org/10.17189/1522643>
- Benison, K. C. (2019). How to search for life in martian chemical sediments and their fluid and solid inclusions using petrographic and spectroscopic methods. *Frontiers in Environmental Science*, 7, 108. <https://doi.org/10.3389/fenvs.2019.00108>
- Benison, K. C., & Karmanocky, F. J., III. (2014). Could microorganisms be preserved in Mars gypsum? Insights from terrestrial examples. *Geology*, 42(7), 615–618. <https://doi.org/10.1130/g35542.1>
- Beysac, O., Forni, O., Cousin, A., Udry, A., Kah, L., Mandon, L., et al. (2023). Petrological traverse of the olivine cumulate Séítah formation at Jezero crater, Mars: A perspective from SuperCam onboard perseverance. *Journal of Geophysical Research: Planets*, 128(7), e2022JE007638. <https://doi.org/10.1029/2022je007638>
- Bhartia, R., Beegle, L. W., DeFlores, L., Abbey, W., Razzell Hollis, J., Uckert, K., et al. (2021). Perseverance’s scanning habitable environments with Raman and luminescence for organics and chemicals (SHERLOC) investigation. *Space Science Reviews*, 217(4), 58. <https://doi.org/10.1007/s11214-021-00812-z>
- Bibring, J. P., Langevin, Y., Mustard, J. F., Poulet, F., Arvidson, R., Gendrin, A., et al. (2006). Global mineralogical and aqueous Mars history derived from OMEGA/Mars Express data. *Science*, 312(5772), 400–404. <https://doi.org/10.1126/science.1122659>
- Bowden, S. A., & Parnell, J. (2007). Intracrystalline lipids within sulfates from the Haughton impact structure—Implications for survival of lipids on Mars. *Icarus*, 187(2), 422–429. <https://doi.org/10.1016/j.icarus.2006.10.013>
- Bridges, J. C., Catling, D., Saxton, J., Swindle, T., Lyon, I., & Grady, M. (2001). Alteration assemblages in Martian meteorites: Implications for near-surface processes. *Space Science Reviews*, 96(1/4), 365–392. <https://doi.org/10.1023/a:1011965826553>
- Chio, C. H., Sharma, S. K., & Muenow, D. W. (2005). Micro-Raman studies of hydrous ferrous sulfates and jarosites. *Spectrochimica Acta Part A: Molecular and Biomolecular Spectroscopy*, 61(10), 2428–2433. <https://doi.org/10.1016/j.saa.2005.02.021>
- Chipera, S. J., & Vaniman, D. T. (2007). Experimental stability of magnesium sulfate hydrates that may be present on Mars. *Geochimica et Cosmochimica Acta*, 71(1), 241–250. <https://doi.org/10.1016/j.gca.2006.07.044>
- Chipera, S. J., Vaniman, D. T., Rampe, E. B., Bristow, T. F., Martínez, G., Tu, V. M., et al. (2023). Mineralogical investigation of Mg-sulfate at the Canaima drill site, Gale crater, Mars. *Journal of Geophysical Research: Planets*, 128(11), e2023JE008041. <https://doi.org/10.1029/2023JE008041>
- Chou, I.-M., & Seal, R. R., II. (2007). Magnesium and calcium sulfate stabilities and the water budget of Mars. *Journal of Geophysical Research*, 112(E11), E11004. <https://doi.org/10.1029/2007JE002898>
- Clark, B. C., & Van Hart, D. C. (1981). The salts of Mars. *Icarus*, 45(2), 370–378. [https://doi.org/10.1016/0019-1035\(81\)90041-5](https://doi.org/10.1016/0019-1035(81)90041-5)
- Clark, J. V., Morris, R. V., Haney, N. C., Jakubek, R. S., Archer, P. D., McAdam, A. C., et al. (2023). Combined thermal and evolved gas analysis, X-ray diffraction, vis-NIR, X-ray fluorescence, and DUV Raman spectroscopy of synthetic amorphous magnesium sulfates and starkeyite: Implications for the detection of Mg sulfates by the sample analysis at Mars instrument in Gale crater, Mars. In *Abstract 2441, presented at the 54th lunar and planetary science conference*.
- Corpolongo, A., Jakubek, R. S., Burton, A. S., Brown, A. J., Yanchilina, A., Czaja, A. D., et al. (2023). SHERLOC Raman mineral class detections of the Mars 2020 Crater Floor campaign. *Journal of Geophysical Research: Planets*, 128(3), e2022JE007455. <https://doi.org/10.1029/2022JE007455>
- Culka, A., Košek, F., Drahot, P., & Jehlička, J. (2014). Use of miniaturized Raman spectrometer for detection of sulfates of different hydration states—Significance for Mars studies. *Icarus*, 243, 440–453. <https://doi.org/10.1016/j.icarus.2014.08.017>
- Dehouck, E., Chevrier, V., Gaudin, A., Mangold, N., Mathé, P. E., & Rochette, P. (2012). Evaluating the role of sulfide-weathering in the formation of sulfates or carbonates on Mars. *Geochimica et Cosmochimica Acta*, 90, 47–63. <https://doi.org/10.1016/j.gca.2012.04.057>
- Dela Pierre, F., Natalicchio, M., Ferrando, S., Giustetto, R., Birgel, D., Carnevale, G., et al. (2015). Are the large filamentous microfossils preserved in Messinian gypsum colorless sulfide-oxidizing bacteria? *Geology*, 43(10), 855–858. <https://doi.org/10.1130/g37018.1>
- Edgett, K. S., Yingst, R. A., Ravine, M. A., Caplinger, M. A., Maki, J. N., Ghaemi, F. T., et al. (2012). Curiosity’s Mars hand lens imager (MAHLI) investigation. *Space Science Reviews*, 170(1–4), 259–317. <https://doi.org/10.1007/s11214-012-9910-4>
- Ehlmann, B. L., & Edwards, C. S. (2014). Mineralogy of the Martian surface. *Annual Review of Earth and Planetary Sciences*, 42(1), 291–315. <https://doi.org/10.1146/annurev-earth-060313-055024>
- Eigenbrode, J. L., Summons, R. E., Steele, A., Freissinet, C., Millan, M., Navarro-González, R., et al. (2018). Organic matter preserved in 3-billion-year-old mudstones at Gale crater, Mars. *Science*, 360(6393), 1096–1101. <https://doi.org/10.1126/science.aas9185>

- Elam, W. T., & Heirwegh, C. M. (2022). PIQUANT Piquant (version v3.2.11). *Zenodo*. <https://doi.org/10.5281/zenodo.6959125>
- Farley, K. A., & Stack, K. M. (2022). Mars 2020 initial reports—Crater Floor campaign. Retrieved from <https://pds-geosciences.wustl.edu/missions/mars2020/Mars2020InitialReports1-10October2022.pdf>
- Farley, K. A., Stack, K. M., Shuster, D. L., Horgan, B. H. N., Hurowitz, J. A., Tarnas, J. D., et al. (2022). Aqueously altered igneous rocks sampled on the floor of Jezero crater, Mars. *Science*, *377*(6614), eabo2196. <https://doi.org/10.1126/science.abo2196>
- Farley, K. A., Williford, K. H., Stack, K. M., Bhartia, R., Chen, A., de la Torre, M., et al. (2020). Mars 2020 mission overview. *Space Science Reviews*, *216*(8), 142. <https://doi.org/10.1007/s11214-020-00762-y>
- Farrand, W. H., Glotch, T. D., Rice, J. W., Hurowitz, J. A., & Swayze, G. A. (2009). Discovery of jarosite within the Mawrth Vallis region of Mars: Implications for the geologic history of the region. *Icarus*, *204*(2), 478–488. <https://doi.org/10.1016/j.icarus.2009.07.014>
- Fassett, C. I., & Head, J. W., III. (2005). Fluvial sedimentary deposits on Mars: Ancient deltas in a crater lake in the Nili Fossae region. *Geophysical Research Letters*, *32*(14), L14201. <https://doi.org/10.1029/2005gl023456>
- Feldman, W. C., Mellon, M. T., Maurice, S., Prettyman, T. H., Carey, J. W., Vaniman, D. T., et al. (2004). Hydrated states of MgSO<sub>4</sub> at equatorial latitudes on Mars. *Geophysical Research Letters*, *31*(16), L16702. <https://doi.org/10.1029/2004gl020181>
- Feldman, W. C., Prettyman, T. H., Maurice, S., Plaut, J. J., Bish, D. L., Vaniman, D. T., et al. (2004). Global distribution of near-surface hydrogen on Mars. *Journal of Geophysical Research*, *109*(E9), E09006. <https://doi.org/10.1029/2003je002160>
- Franz, H. B., McAdam, A. C., Ming, D. W., Freissinet, C., Mahaffy, P. R., Eldridge, D. L., et al. (2017). Large sulfur isotope fractionations in Martian sediments at Gale crater. *Nature Geoscience*, *10*(9), 658–662. <https://doi.org/10.1038/ngeo3002>
- Gaft, M., & Raichlin, Y. (2020). Luminescence of 5d–4f transitions of Pr<sup>3+</sup> in natural fluorite CaF<sub>2</sub>, anhydrite CaSO<sub>4</sub> and apatite Ca<sub>5</sub>(PO<sub>4</sub>)<sub>3</sub>F. *Physics and Chemistry of Minerals*, *47*(5), 5. <https://doi.org/10.1007/s00269-019-01074-6>
- Gendrin, A., Mangold, N., Bibring, J.-P., Langevin, Y., Gondet, B., Poulet, F., et al. (2005). Sulfates in martian layered terrains: The OMEGA/Mars express view. *Science*, *307*(5715), 1587–1591. <https://doi.org/10.1126/science.1109087>
- Gill, K. K., Jagnicki, E. A., Benison, K. C., & Gibson, M. E. (2023). A Mars-analog sulfate mineral, mirabilite, preserves biosignatures. *Geology*, *51*(9), 818–822. <https://doi.org/10.1130/G51256.1>
- Goudge, T. A., Mustard, J. F., Head, J. W., Fassett, C. I., & Wiseman, S. M. (2015). Assessing the mineralogy of the watershed and fan deposits of the Jezero crater paleolake system, Mars. *Journal of Geophysical Research: Planets*, *120*(4), 775–808. <https://doi.org/10.1002/2014je004782>
- Gough, R., Chevrier, V., Baustian, K., Wise, M., & Tolbert, M. (2011). Laboratory studies of perchlorate phase transitions: Support for metastable aqueous perchlorate solutions on Mars. *Earth and Planetary Science Letters*, *312*(3–4), 371–377. <https://doi.org/10.1016/j.epsl.2011.10.026>
- Hamilton, A., & Menzies, R. I. (2010). Raman spectra of mirabilite, Na<sub>2</sub>SO<sub>4</sub>·10H<sub>2</sub>O and the rediscovered metastable heptahydrate, Na<sub>2</sub>SO<sub>4</sub>·7H<sub>2</sub>O. *Journal of Raman Spectroscopy*, *41*(9), 1014–1020. <https://doi.org/10.1002/jrs.2547>
- Hamran, S.-E., Paige, D. A., Allwood, A., Amundsen, H. E., Berger, T., Brovill, S., et al. (2022). Ground penetrating radar observations of subsurface structures in the floor of Jezero crater, Mars. *Science Advances*, *8*(34), eabp8564. <https://doi.org/10.1126/sciadv.abp8564>
- Hausrath, E. M., Adcock, C. T., Bechtold, A., Beck, P., Benison, K., Brown, A., et al. (2023). An examination of soil crusts on the floor of Jezero crater, Mars. *Journal of Geophysical Research: Planets*, *128*(10), e2022JE007433. <https://doi.org/10.1029/2022JE007433>
- Hausrath, E. M., & Brantley, S. L. (2010). Basalt and olivine dissolution under cold, salty, and acidic conditions: What can we learn about recent aqueous weathering on Mars? *Journal of Geophysical Research*, *115*(E12), E12001. <https://doi.org/10.1029/2010je003610>
- Hausrath, E. M., Navarre-Sitchler, A. K., Sak, P. B., Steefel, C. I., & Brantley, S. L. (2008). Basalt weathering rates on Earth and the duration of liquid water on the plains of Gusev Crater, Mars. *Geology*, *36*(1), 67–70. <https://doi.org/10.1130/g24238a.1>
- Heirwegh, C., Elam, W., O'Neil, L., Sinclair, K., & Das, A. (2022). The focused beam X-ray fluorescence elemental quantification software package PIQUANT. *Spectrochimica Acta Part B: Atomic Spectroscopy*, *196*, 106520. <https://doi.org/10.1016/j.sab.2022.106520>
- Holm-Alwmark, S., Kinch, K., Hansen, M., Shahrzad, S., Svennevig, K., Abbey, W., et al. (2021). Stratigraphic relationships in Jezero crater, Mars: Constraints on the timing of fluvial-lacustrine activity from orbital observations. *Journal of Geophysical Research: Planets*, *126*(7), e2021JE006840. <https://doi.org/10.1029/2021je006840>
- Horgan, B. H. N., Udry, A., Rice, M. S., Alwmark, S., Amundsen, H. E., Bell, J. F., III, et al. (2023). Mineralogy, morphology, and emplacement history of the Maaz formation on the Jezero crater floor from orbital and rover observations. *Authorea Preprints*. <https://doi.org/10.1002/essoar.10512674.1>
- Huang, W., Ertekin, E., Wang, T., Cruz, L., Dailey, M., DiRuggiero, J., & Kisailus, D. (2020). Mechanism of water extraction from gypsum rock by desert colonizing microorganisms. *Proceedings of the National Academy of Sciences*, *117*(20), 10681–10687. <https://doi.org/10.1073/pnas.2001613117>
- Hurowitz, J. A., Tice, M. M., Allwood, A. C., Cable, M. L., Bosak, T., Broz, A., et al. (2023). The petrogenetic history of the Jezero Crater delta front from microscale observations by the Mars 2020 PIXL instrument. In *Paper presented at the 54th lunar and planetary science conference*.
- Kah, L. C., Stack, K. M., Eigenbrode, J. L., Yingst, R. A., & Edgett, K. S. (2018). Syndepositional precipitation of calcium sulfate in Gale crater, Mars. *Terra Nova*, *30*(6), 431–439. <https://doi.org/10.1111/ter.12359>
- Karunatillake, S., Wray, J., Gasnault, O., McLennan, S., Rogers, A., Squyres, S., et al. (2014). Sulfates hydrating bulk soil in the Martian low and middle latitudes. *Geophysical Research Letters*, *41*(22), 7987–7996. <https://doi.org/10.1002/2014gl061136>
- Karunatillake, S., Wray, J. J., Gasnault, O., McLennan, S. M., Deanne Rogers, A., Squyres, S. W., et al. (2016). The association of hydrogen with sulfur on Mars across latitudes, longitudes, and compositional extremes. *Journal of Geophysical Research: Planets*, *121*(7), 1321–1341. <https://doi.org/10.1002/2016je005016>
- Klingelhöfer, G., Morris, R. V., Bernhardt, B., Schröder, C., Rodionov, D. S., de Souza, P. A., et al. (2004). Jarosite and hematite at Meridiani Planum from opportunity's Mössbauer spectrometer. *Science*, *306*(5702), 1740–1745. <https://doi.org/10.1126/science.1104653>
- Kounaves, S. P., Hecht, M. H., Kapit, J., Quinn, R. C., Catling, D. C., Clark, B. C., et al. (2010). Soluble sulfate in the martian soil at the Phoenix landing site. *Geophysical Research Letters*, *37*(9), L09201. <https://doi.org/10.1029/2010GL042613>
- Kronyak, R. E., Kah, L. C., Edgett, K. S., VanBommel, S. J., Thompson, L. M., Wiens, R. C., et al. (2019). Mineral-filled fractures as indicators of multigenerational fluid flow in the Pahrump Hills member of the Murray formation, Gale crater, Mars. *Earth and Space Science*, *6*(2), 238–265. <https://doi.org/10.1029/2018EA000482>
- Lide, D. R. (2004). *CRC handbook of chemistry and physics* (Vol. 85). CRC Press.
- Liu, Y., Tice, M., Schmidt, M., Treiman, A., Kizovski, T., Hurowitz, J., et al. (2022). An olivine cumulate outcrop on the floor of Jezero crater, Mars. *Science*, *377*(6614), 1513–1519. <https://doi.org/10.1126/science.abo2756>
- Lowenstein, T. K., Schubert, B. A., & Timofeeff, M. N. (2011). Microbial communities in fluid inclusions and long-term survival in halite. *Geological Society of America Today*, *21*(1), 4–9. <https://doi.org/10.1130/gsatg81a.1>
- Mandon, L., Quantin-Nataf, C., Royer, C., Beck, P., Fouchet, T., Johnson, J., et al. (2023). Reflectance of Jezero crater floor: 2. Mineralogical interpretation. *Journal of Geophysical Research: Planets*, *128*(7), e2022JE007450. <https://doi.org/10.1029/2022je007450>

- Mandon, L., Quantin-Nataf, C., Thollot, P., Mangold, N., Lozac'h, L., Dromart, G., et al. (2020). Refining the age, emplacement and alteration scenarios of the olivine-rich unit in the Nili Fossae region, Mars. *Icarus*, 336, 113436. <https://doi.org/10.1016/j.icarus.2019.113436>
- Mangold, N., Dromart, G., Ansan, V., Salese, F., Kleinhans, M. G., Massé, M., et al. (2020). Fluvial regimes, morphometry, and age of Jezero crater paleolake inlet valleys and their exobiological significance for the 2020 Rover Mission Landing Site. *Astrobiology*, 20(8), 994–1013. <https://doi.org/10.1089/ast.2019.2132>
- Marion, G., Catling, D., Kargel, J., & Crowley, J. (2016). Modeling calcium sulfate chemistries with applications to Mars. *Icarus*, 278, 31–37. <https://doi.org/10.1016/j.icarus.2016.05.016>
- Martínez, G. M., Sebastián, E., Vicente-Retortillo, A., Smith, M. D., Johnson, J. R., Fischer, E., et al. (2023). Surface energy budget, albedo, and thermal inertia at Jezero Crater, Mars, as observed from the Mars 2020 MEDA instrument. *Journal of Geophysical Research: Planets*, 128(2), e2022JE007537. <https://doi.org/10.1029/2022je007537>
- Martín-Torres, F. J., Zorzano, M.-P., Valentín-Serrano, P., Harri, A.-M., Genzer, M., Kemppinen, O., et al. (2015). Transient liquid water and water activity at Gale crater on Mars. *Nature Geoscience*, 8(5), 357–361. <https://doi.org/10.1038/ngeo2412>
- McCullom, T. M. (2018). Geochemical trends in the Burns formation layered sulfate deposits at Meridiani Planum, Mars, and implications for their origin. *Journal of Geophysical Research: Planets*, 123(9), 2393–2429. <https://doi.org/10.1029/2018JE005718>
- McCullom, T. M., & Hynes, B. (2021). Geochemical data indicate highly similar sediment compositions for the Grasberg and Burns formations on Meridiani Planum, Mars. *Earth and Planetary Science Letters*, 557, 116729. <https://doi.org/10.1016/j.epsl.2020.116729>
- McCubbin, F. M., Tosca, N. J., Smirnov, A., Nekvasil, H., Steele, A., Fries, M., & Lindsley, D. H. (2009). Hydrothermal jarosite and hematite in a pyroxene-hosted melt inclusion in martian meteorite Miller Range (MIL) 03346: Implications for magmatic-hydrothermal fluids on Mars. *Geochimica et Cosmochimica Acta*, 73(16), 4907–4917. <https://doi.org/10.1016/j.gca.2009.05.031>
- McLennan, S. M. (2012). Geochemistry of sedimentary processes on Mars. In J. P. Grotzinger & R. E. Milliken (Eds.), *Sedimentary geology of Mars*. SEPM. <https://doi.org/10.2110/pec.12.102.0119>
- McLennan, S. M., Bell, J. F., Calvin, W. M., Christensen, P. R., Clark, B. C., de Souza, P. A., et al. (2005). Provenance and diagenesis of the evaporite-bearing Burns formation, Meridiani Planum, Mars. *Earth and Planetary Science Letters*, 240(1), 95–121. <https://doi.org/10.1016/j.epsl.2005.09.041>
- Mees, F., Casteneda, C., Herrero, J., & Van Ranst, E. (2012). The nature and significance of variations in gypsum crystal morphology in dry lake basins. *Journal of Sedimentary Research*, 82(1), 37–52. <https://doi.org/10.2110/jsr.2012.3>
- Millan, M., Teinturier, S., Malespin, C., Bonnet, J., Buch, A., Dworkin, J., et al. (2022). Organic molecules revealed in Mars's Bagnold Dunes by Curiosity's derivatization experiment. *Nature Astronomy*, 6(1), 129–140. <https://doi.org/10.1038/s41550-021-01507-9>
- Miller, K. (2017). *Anhydrite nucleation and growth at low temperatures: Effects of flow rate, activity of water, and mineral substrates*. (Master's thesis). University of Oklahoma. Retrieved from <https://shareok.org/handle/11244/50862>
- Milliken, R. E., Grotzinger, J. P., & Thomson, B. J. (2010). Paleoclimate of Mars as captured by the stratigraphic record in Gale crater. *Geophysical Research Letters*, 37(4), L04201. <https://doi.org/10.1029/2009GL041870>
- Moore, R. D., & Szykiewicz, A. (2023). Aqueous sulfate contributions in terrestrial basaltic catchments: Implications for understanding sulfate sources and transport in Meridiani Planum, Mars. *Icarus*, 391, 115342. <https://doi.org/10.1016/j.icarus.2022.115342>
- Morris, R. V., Klingelhöfer, G., Schröder, C., Rodionov, D. S., Yen, A., Ming, D. W., et al. (2006). Mössbauer mineralogy of rock, soil, and dust at Gusev crater, Mars: Spirit's journey through weakly altered olivine basalt on the plains and pervasively altered basalt in the Columbia Hills. *Journal of Geophysical Research*, 111(E2), E02S13. <https://doi.org/10.1029/2005JE002584>
- Mustard, J. F. (2019). Sequestration of volatiles in the martian crust through hydrated minerals: A significant planetary reservoir of water. In *Volatiles in the martian crust* (pp. 247–263). Elsevier.
- Nachon, M., Clegg, S., Mangold, N., Schröder, S., Kah, L., Dromart, G., et al. (2014). Calcium sulfate veins characterized by ChemCam/Curiosity at Gale crater, Mars. *Journal of Geophysical Research: Planets*, 119(9), 1991–2016. <https://doi.org/10.1002/2013je004588>
- Nemere, P., Barber, T., Galvin, A., Wright, A. P., Fedell, S. M., Stonebraker, R., et al. (2022a). PIXLISE core (version v2.0). *Zenodo*. <https://doi.org/10.5281/zenodo.6959096>
- Nemere, P., Barber, T., Galvin, A., Wright, A. P., Fedell, S. M., Stonebraker, R., et al. (2022b). PIXLISE UI (Version v2.0). *Zenodo*. <https://doi.org/10.5281/zenodo.6959109>
- Ono, S. (2017). Photochemistry of sulfur dioxide and the origin of mass-independent isotope fractionation in Earth's atmosphere. *Annual Review of Earth and Planetary Sciences*, 45(1), 301–329. <https://doi.org/10.1146/annurev-earth-060115-012324>
- Pedersen, D. A. K., Henneke, J., Liu, Y., Tosca, N., Tice, M. M., Joergensen, J. L., et al. (2022). PIXL's multispectral observations in Jezero Crater. In *Paper presented at the 2022 American geophysical union fall meeting*.
- Peterson, R. C., & Wang, R. (2006). Crystal molds on Mars: Melting of a possible new mineral species to create Martian chaotic terrain. *Geology*, 34(11), 957–960. <https://doi.org/10.1130/g22678a.1>
- Phua, Y., Ehlmann, B. L., Mandon, L., Siljeström, S., Razzell Hollis, J., & Bhartia, R. (2023). Characterizing hydration in alteration minerals of Jezero Crater geologic units with SHERLOC on Mars 2020. In *Paper presented at the 54th annual lunar and planetary science conference (LPI contrib. no. 2806)*.
- Polkko, J., Hieta, M., Harri, A. M., Tamppari, L., Martínez, G., Viúdez-Moreiras, D., et al. (2023). Initial results of the relative humidity observations by MEDA instrument onboard the Mars 2020 Perseverance Rover. *Journal of Geophysical Research: Planets*, 128(2), e2022JE007447. <https://doi.org/10.1029/2022je007447>
- Rampe, E. B., Blake, D. F., Bristow, T., Ming, D. W., Vaniman, D., Morris, R., et al. (2020). Mineralogy and geochemistry of sedimentary rocks and eolian sediments in Gale crater, Mars: A review after six earth years of exploration with curiosity. *Geochemistry*, 80(2), 125605. <https://doi.org/10.1016/j.chemer.2020.125605>
- Rapin, W., Ehlmann, B. L., Dromart, G., Schieber, J., Thomas, N., Fischer, W. W., et al. (2019). An interval of high salinity in ancient Gale crater lake on Mars. *Nature Geoscience*, 12(11), 889–895. <https://doi.org/10.1038/s41561-019-0458-8>
- Razzell Hollis, J., Abbey, W., Beegle, L. W., Bhartia, R., Ehlmann, B. L., Miura, J., et al. (2021). A deep-ultraviolet Raman and Fluorescence spectral library of 62 minerals for the SHERLOC instrument onboard Mars 2020. *Planetary and Space Science*, 209, 105356. <https://doi.org/10.1016/j.pss.2021.105356>
- Razzell Hollis, J., Moore, K. R., Sharma, S., Beegle, L., Grotzinger, J. P., Allwood, A., et al. (2022). The power of paired proximity science observations: Co-located data from SHERLOC and PIXL on Mars. *Icarus*, 387, 115179. <https://doi.org/10.1016/j.icarus.2022.115179>
- Robertson, K., & Bish, D. (2013). Constraints on the distribution of CaSO<sub>4</sub>·nH<sub>2</sub>O phases on Mars and implications for their contribution to the hydrological cycle. *Icarus*, 223(1), 407–417. <https://doi.org/10.1016/j.icarus.2012.10.028>
- Rodriguez-Manfredi, J. A., de la Torre Juárez, M., Mora Sotomayor, L., Deen, R. G., Algermissen, S., Dunn, A. E., et al. (2021). Mars 2020 MEDA bundle. *NASA Planetary Data System*. <https://doi.org/10.17189/1522849>



- Roppel, R. D., Abbey, W. J., Asher, S. A., Bhartia, R., Bykov, S. V., Conrad, P., et al. (2023). Investigation of mineralogies during the delta front campaign by SHERLOC. In *Paper presented at the 54th annual lunar and planetary science conference (LPI contrib. no. 2806)*.
- Scheller, E. L., Ehlmann, B. L., Hu, R., Adams, D. J., & Yung, Y. L. (2021). Long-term drying of Mars by sequestration of ocean-scale volumes of water in the crust. *Science*, *372*(6537), 56–62. <https://doi.org/10.1126/science.abc7717>
- Scheller, E. L., Hollis, J. R., Cardarelli, E. L., Steele, A., Beegle, L. W., Bhartia, R., et al. (2022). Aqueous alteration processes in Jezero crater, Mars—Implications for organic geochemistry. *Science*, *378*(0), eabo5204.
- Schmidt, M., Allwood, A., Christian, J., Clark, B., Flannery, D., Hennecke, J., et al. (2022). Highly differentiated basaltic lavas examined by PIXL in Jezero crater. In *Paper presented at the proceedings of the 53rd lunar and planetary science conference (LPSC)*.
- Schon, S. C., Head, J. W., & Fassett, C. I. (2012). An overfilled lacustrine system and progradational delta in Jezero crater, Mars: Implications for Noachian climate. *Planetary and Space Science*, *67*(1), 28–45. <https://doi.org/10.1016/j.pss.2012.02.003>
- Schopf, J. W., Farmer, J. D., Foster, I. S., Kudryavtsev, A. B., Gallardo, V. A., & Espinoza, C. (2012). Gypsum-permineralized microfossils and their relevance to the search for life on Mars. *Astrobiology*, *12*(7), 619–633. <https://doi.org/10.1089/ast.2012.0827>
- Schredder-Gomes, S. I., Benison, K. C., & Bernau, J. A. (2022). 830-million-year-old microorganisms in primary fluid inclusions in halite. *Geology*, *50*(8), 918–922. <https://doi.org/10.1130/g49957.1>
- Seal, R. R., Alpers, C. N., & Rye, R. O. (2000). Stable isotope systematics of sulfate minerals. *Reviews in Mineralogy and Geochemistry*, *40*(1), 541–602. <https://doi.org/10.2138/rmg.2000.40.12>
- Sharma, S., Roppel, R. D., Murphy, A. E., Beegle, L. W., Bhartia, R., Steele, A., et al. (2023). Diverse organic-mineral associations in Jezero crater, Mars. *Nature*, *619*(7971), 724–732. <https://doi.org/10.1038/s41586-023-06143-z>
- Simon, J. I., Hickman-Lewis, K., Cohen, B. A., Mayhew, L. E., Shuster, D. L., Debaille, V., et al. (2023). Samples collected from the floor of Jezero Crater with the Mars 2020 perseverance rover. *Journal of Geophysical Research: Planets*, *128*(6), e2022JE007474. <https://doi.org/10.1029/2022JE007474>
- Smith, R., McLennan, S., Sutter, B., Rampe, E., Dehouck, E., Siebach, K., et al. (2022). X-ray amorphous sulfur-bearing phases in sedimentary rocks of Gale crater, Mars. *Journal of Geophysical Research: Planets*, *127*(5), e2021JE007128. <https://doi.org/10.1029/2021je007128>
- Stack, K. M., Williams, N. R., Calef, F., Sun, V. Z., Williford, K. H., Farley, K. A., et al. (2020). Photogeologic map of the perseverance rover field site in Jezero Crater constructed by the Mars 2020 science team. *Space Science Reviews*, *216*(8), 127. <https://doi.org/10.1007/s11214-020-00739-x>
- Sun, V. Z., Hand, K. P., Stack, K. M., Farley, K. A., Simon, J. I., Newman, C., et al. (2023). Overview and results from the Mars 2020 perseverance Rover's first science campaign on the Jezero Crater Floor. *Journal of Geophysical Research: Planets*, *128*(6), e2022JE007613. <https://doi.org/10.1029/2022je007613>
- Sun, V. Z., & Stack, K. M. (2020). *Geologic map of Jezero crater and the Nili Planum region*. Mars: US Department of the Interior, US Geological Survey.
- Talla, D., & Wildner, M. (2019). Investigation of the kieserite–szomolnokite solid-solution series, (Mg,Fe)SO<sub>4</sub>·H<sub>2</sub>O, with relevance to Mars: Crystal chemistry, FTIR, and Raman spectroscopy under ambient and martian temperature conditions. *American Mineralogist: Journal of Earth and Planetary Materials*, *104*(12), 1732–1749. <https://doi.org/10.2138/am-2019-6983>
- Tan, J., & Sephton, M. A. (2020). Organic records of early life on Mars: The role of iron, burial and kinetics on preservation. *Astrobiology*, *20*(1), 53–72. <https://doi.org/10.1089/ast.2019.2046>
- Tice, M. M., Hurowitz, J. A., Allwood, A. C., Jones, M. W., Orenstein, B. J., Davidoff, S., et al. (2022). Alteration history of Séítah formation rocks inferred by PIXL x-ray fluorescence, x-ray diffraction, and multispectral imaging on Mars. *Science Advances*, *8*(47), eabp9084. <https://doi.org/10.1126/sciadv.abp9084>
- Tice, M. M., O'Neil, L. P., Clark, B. C., Ganly, B. P., Jones, M. W. M., Orenstein, B. J., et al. (2023). PIXL on perseverance as a complete X-ray spectroscopic instrument: Analyzing X-ray fluorescence, scattering, and diffraction in martian rocks. In *Paper presented at the 54th annual lunar and planetary science conference (LPI contrib. no. 2806)*.
- Toner, J. D., & Catling, D. C. (2016). Water activities of NaClO<sub>4</sub>, Ca(ClO<sub>4</sub>)<sub>2</sub>, and Mg(ClO<sub>4</sub>)<sub>2</sub> brines from experimental heat capacities: Water activity >0.6 below 200 K. *Geochimica et Cosmochimica Acta*, *181*, 164–174. <https://doi.org/10.1016/j.gca.2016.03.005>
- Tosca, N. J., Knoll, A. H., & McLennan, S. M. (2008). Water activity and the challenge for life on early Mars. *Science*, *320*(5880), 1204–1207. <https://doi.org/10.1126/science.1155432>
- Tosca, N. J., & McLennan, S. M. (2006). Chemical divides and evaporite assemblages on Mars. *Earth and Planetary Science Letters*, *241*(1–2), 21–31. <https://doi.org/10.1016/j.epsl.2005.10.021>
- Tosca, N. J., McLennan, S. M., Lindsley, D. H., & Schoonen, M. A. (2004). Acid-sulfate weathering of synthetic Martian basalt: The acid fog model revisited. *Journal of Geophysical Research*, *109*(E5). <https://doi.org/10.1029/2003je002218>
- Uckert, K. (2022). Loupe (version V5.1.5). *Zenodo*. <https://doi.org/10.5281/zenodo.7062998>
- Udry, A., Ostwald, A., Sautter, V., Cousin, A., Beyssac, O., Forni, O., et al. (2023). A Mars 2020 perseverance SuperCam perspective on the igneous nature of the Máaz Formation at Jezero Crater and link with Séítah, Mars. *Journal of Geophysical Research: Planets*, *128*(7), e2022JE007440. <https://doi.org/10.1029/2022je007440>
- Vaniman, D. T., Bish, D. L., Chipera, S. J., Fialips, C. I., William Carey, J., & Feldman, W. C. (2004). Magnesium sulphate salts and the history of water on Mars. *Nature*, *431*(7009), 663–665. <https://doi.org/10.1038/nature02973>
- Vaniman, D. T., & Chipera, S. J. (2006). Transformations of Mg- and Ca-sulfate hydrates in Mars regolith. *American Mineralogist*, *91*(10), 1628–1642. <https://doi.org/10.2138/am.2006.2092>
- Vaniman, D. T., Martínez, G. M., Rampe, E. B., Bristow, T. F., Blake, D. F., Yen, A. S., et al. (2018). Gypsum, bassanite, and anhydrite at Gale crater, Mars. *American Mineralogist*, *103*(7), 1011–1020. <https://doi.org/10.2138/am-2018-6346>
- Wang, A., Freeman, J., Chou, I. M., & Jolliff, B. (2011). Stability of Mg-sulfates at –10° C and the rates of dehydration/rehydration processes under conditions relevant to Mars. *Journal of Geophysical Research*, *116*(E12), E12006. <https://doi.org/10.1029/2011je003818>
- Wang, A., Freeman, J. J., & Jolliff, B. L. (2009). Phase transition pathways of the hydrates of magnesium sulfate in the temperature range 50°C to 5°C: Implication for sulfates on Mars. *Journal of Geophysical Research*, *114*(E4), C05006. <https://doi.org/10.1029/2008je003266>
- Wang, A., Freeman, J. J., Jolliff, B. L., & Chou, I.-M. (2006). Sulfates on Mars: A systematic Raman spectroscopic study of hydration states of magnesium sulfates. *Geochimica et Cosmochimica Acta*, *70*(24), 6118–6135. <https://doi.org/10.1016/j.gca.2006.05.022>
- Wang, A., Haskin, L. A., Squyres, S. W., Jolliff, B. L., Crumpler, L., Gellert, R., et al. (2006). Sulfate deposition in subsurface regolith in Gusev crater, Mars. *Journal of Geophysical Research*, *111*(E2), E02S17. <https://doi.org/10.1029/2005JE002513>
- Wang, A., Jolliff, B. L., Liu, Y., & Connor, K. (2016). Setting constraints on the nature and origin of the two major hydrous sulfates on Mars: Monohydrated and polyhydrated sulfates. *Journal of Geophysical Research: Planets*, *121*(4), 678–694. <https://doi.org/10.1002/2015je004889>
- Watson, A. (1985). Structure, chemistry and origins of gypsum crusts in southern Tunisia and the central Namib Desert. *Sedimentology*, *32*(6), 855–875. <https://doi.org/10.1111/j.1365-3091.1985.tb00737.x>

- Werner, S. C. (2008). The early martian evolution—Constraints from basin formation ages. *Icarus*, *195*(1), 45–60. <https://doi.org/10.1016/j.icarus.2007.12.008>
- Wierzchos, J., Cámara, B., De Los Ríos, A., Davila, A. F., Sánchez Almazo, I. M., Artieda, O., et al. (2011). Microbial colonization of Ca-sulfate crusts in the hyperarid core of the Atacama desert: Implications for the search for life on Mars. *Geobiology*, *9*(1), 44–60. <https://doi.org/10.1111/j.1472-4669.2010.00254.x>
- Williford, K. H., Farley, K. A., Stack, K. M., Allwood, A. C., Beaty, D., Beegle, L. W., et al. (2018). The NASA Mars 2020 rover mission and the search for extraterrestrial life. In *From habitability to life on Mars* (pp. 275–308). Elsevier.
- Wogsland, B. V., Miniti, M. E., Kah, L. C., Yingst, R. A., Abbey, W., Bhartia, R., et al. (2023). Science and science-enabling activities of the SHERLOC and WATSON imaging systems in Jezero Crater, Mars. *Earth and Space Science*, *10*(11), e2022EA002544. <https://doi.org/10.1029/2022EA002544>
- Wojdyr, M. (2010). Fityk: A general-purpose peak fitting program. *Journal of Applied Crystallography*, *43*(5), 1126–1128. <https://doi.org/10.1107/s0021889810030499>
- Wright, A. P., Nemere, P., Galvin, A., & Davidoff, S. (2022). PIXLISE diffraction detection (version v2.0). *Zenodo*. <https://doi.org/10.5281/zenodo.6959138>
- Zorzano, M. P., Mateo-Martí, E., Prieto-Ballesteros, O., Osuna, S., & Renno, N. (2009). Stability of liquid saline water on present day Mars. *Geophysical Research Letters*, *36*(20), L20201. <https://doi.org/10.1029/2009gl040315>

## References From the Supporting Information

- Abbey, W. J., Bhartia, R., Beegle, L. W., DeFlores, L., Paez, V., Sijapati, K., et al. (2017). Deep UV Raman spectroscopy for planetary exploration: The search for in situ organics. *Icarus*, *290*, 201–214. <https://doi.org/10.1016/j.icarus.2017.01.039>
- Fries, M. D., Lee, C., Bhartia, R., Razzell Hollis, J., Beegle, L. W., Uckert, K., et al. (2022). The SHERLOC calibration target on the Mars 2020 perseverance rover: Design, operations, outreach, and future human exploration functions. *Space Science Reviews*, *218*(6), 46. <https://doi.org/10.1007/s11214-022-00907-1>
- Lenz, D. D., & Ayres, T. R. (1992). Errors associated with fitting Gaussian Profiles to noisy emission-line spectra. *Publications of the Astronomical Society of the Pacific*, *104*(681), 1104–1106. <https://doi.org/10.1086/133096>
- Razzell Hollis, J., Rheingold, D., Bhartia, R., & Beegle, L. W. (2020). An optical model for quantitative Raman microspectroscopy. *Applied Spectroscopy*, *74*(6), 684–700. <https://doi.org/10.1177/0003702819895299>
- Uckert, K., Bhartia, R., Beegle, L. W., Monacelli, B., Asher, S. A., Burton, A. S., et al. (2021). Calibration of the SHERLOC deep ultraviolet fluorescence–Raman spectrometer on the Perseverance Rover. *Applied Spectroscopy*, *75*(7), 763–773. <https://doi.org/10.1177/00037028211013368>